TU Delft

Delft University of Technology

Document Version
Final published version

Licence
Dutch Copyright Act (Article 25fa)

Citation (APA)
Gallardo, J. A., Chacón, M. F., Muñoz, J. P., Gutiérrez-Urzúa, F., Cembrano, J., Rossetto, T., Freddi, F., Crempien, J. G. F., & de la Llera, J. C. (2026). Earthquake Response Sensitivity of HDRB Base-Isolated Hospitals to the Crustal San Ramón Fault in Santiago, Chile. *Earthquake Engineering and Structural Dynamics*, *55*(8), 1631-1654. https://doi.org/10.1002/eqe.70154

Important note
To cite this publication, please use the final published version (if applicable).
Please check the document version above.

Copyright
In case the licence states “Dutch Copyright Act (Article 25fa)”, this publication was made available Green Open Access via the TU Delft Institutional Repository pursuant to Dutch Copyright Act (Article 25fa, the Taverne amendment). This provision does not affect copyright ownership.
Unless copyright is transferred by contract or statute, it remains with the copyright holder.

Sharing and reuse
Other than for strictly personal use, it is not permitted to download, forward or distribute the text or part of it, without the consent of the author(s) and/or copyright holder(s), unless the work is under an open content license such as Creative Commons.

Takedown policy
Please contact us and provide details if you believe this document breaches copyrights.
We will remove access to the work immediately and investigate your claim.

This work is downloaded from Delft University of Technology.

Check for updates

Earthquake Engineering & Structural Dynamics

WILEY

RESEARCH ARTICLE

Earthquake Response Sensitivity of HDRB Base-Isolated Hospitals to the Crustal San Ramón Fault in Santiago, Chile

José A. Gallardo[1,2] | Matías F. Chacón[3] | Juan P. Muñoz[2] | Fernando Gutiérrez-Urzúa[4] | José Cembrano[1] | Tiziana Rossetto[5] | Fabio Freddi[4] | Jorge G. F. Crempien[1,2,6] | Juan C. de la Llera[1,2]

[1]Department of Structural and Geotechnical Engineering, Pontificia Universidad Católica de Chile, Santiago, Chile | [2]Research Center for Integrated Disaster Risk Management (CIGIDEN), Santiago, Chile | [3]Department of Civil Engineering, Universidad Católica de la Santísima Concepción, Concepción, Chile | [4]Department of Civil, Environmental & Geomatic Engineering, University College London, London, UK | [5]Department of Hydraulic Engineering, Technische Universiteit Delft, Delft, the Netherlands | [6]Center for Interdisciplinary Research on Disaster Risk, Resilience and Recovery (CIGIDEN R+), Santiago, Chile

Correspondence: José A. Gallardo (jogallardo@uc.cl) | Juan P. Muñoz (jpmunoz4@uc.cl)

Received: 10 November 2025 | **Revised:** 15 January 2026 | **Accepted:** 27 January 2026

Keywords: base-isolated hospital | crustal earthquakes | high damping rubber bearing | physics-based earthquake simulation | San Ramón fault | seismic vulnerability | sensitivity assessment

ABSTRACT

Subduction megathrust events dominate seismicity in Chile, leading to a less comprehensive understanding of the hazard posed by crustal faults. One such source is the San Ramón fault (SRF), a potentially active fault at the eastern border of the Metropolitan Region of Santiago. This study assesses the seismic performance of three modern hospitals seismically isolated with high damping rubber bearings, located 7–24 km from the SRF trace. Their responses were evaluated using nonlinear 3D finite element models subjected to a suite of 432 synthetic ground motions. To account for the uncertainty in the seismogenic capacity of the SRF, these physics-based simulations systematically vary key source parameters, including event magnitude, average rupture velocity, and corner frequency. For facilities near the fault, the results show critical performance failures. Isolation systems are prone to pounding as displacements exceed their design limits, while large vertical accelerations cause a high probability of tensile forces in the bearings. Furthermore, interstory drifts and floor accelerations in the superstructures exceed the thresholds required to maintain continuous operation. These findings reveal that even the new generation of seismically isolated hospitals is critically vulnerable to near-fault crustal earthquakes if not explicitly designed for them. This unaccounted-for seismic hazard highlights an urgent need for comprehensive risk re-assessment and the development of targeted mitigation strategies in Santiago and other cities facing similar hazards.

1 | Introduction

Chile is located along the active subduction zone between the Nazca and South American plates, which converge at approximately 65.5 mm per year [1]. This subduction interface has the potential to generate seismic events with different characteristics, including short- and long-term slow slip events in the deeper zones, extremely low frequency events in the upper zone, and the well-known megathrust earthquakes [2]. Among these, the latter are the most frequent and have strongly influenced the development of Chilean seismic codes, design standards, and urban infrastructure. Significant earthquakes that have shaped the Chilean history include the 1906 Valparaíso Earthquake, which led to the creation of a Seismological Observatory in 1908 [3]; the 1960 Valdivia earthquake, the largest seismic event ever recorded [3]; the 1985 Valparaíso earthquake, whose ground motion (GM) data were used for calibrating the design spectra of current seismic standards; and the 2010 Maule earthquake, after

© 2026 John Wiley & Sons Ltd.

which health authorities promoted the use of seismic isolation in new hospital structures [4, 5]. This policy led to a new generation of base-isolated (BI) hospitals being built across the Metropolitan Region of Santiago (MRS) and the rest of Chile, all analyzed and designed assuming seismic hazards defined by these historical megathrust subduction events. However, the impact of GMs from other seismic sources on these critical facilities and other essential infrastructure remains unknown.

Recent studies show that the MRS is exposed to a seismic hazard from the San Ramón fault (SRF) in addition to the subduction interface. This potentially active crustal fault [6] is located at the eastern border of the capital city, at the piedmont of the Andes mountain range [7]. The SRF trace runs for about 35 km in the north–south direction, extending from the Mapocho river in the north to the Maipo river in the south [6, 8]. Its trace is split into four segments with a mean length of 10 km [9]. In addition to its along-strike segmentation, the fault has local kinematic complexity, including normal, strike-slip, and thrust subfaults, as well as potentially creeping regions. This complexity, combined with limited historical data, means the seismogenic capacity of the SRF is poorly understood, creating significant uncertainty in key source parameters essential for reliable seismic hazard assessment. Furthermore, given the proximity of the fault trace to the community, earthquakes generated by this source could significantly affect essential structures and infrastructure, compromising their ability to meet their expected seismic performance. This is especially concerning for essential facilities like hospitals, whose continuous operation must be ensured for an effective community response and recovery after a seismic event [10].

The new generation of Chilean hospitals is designed with seismic isolation to ensure continuous operativity even after severe seismic events, mainly using high damping rubber bearings (HDRBs) sometimes supplemented by frictional sliders (SLs). While this technology offers enhanced protection, previous studies have shown that GMs from crustal faults can generate significantly larger demands on both the isolation system and the superstructure compared to spectrally equivalent GMs from megathrust earthquakes [11–13]. Previous studies have demonstrated that long-period velocity pulses—inherent to directionality effects of near-fault GMs—can impose large displacement demands [14, 15], which potentially can exceed the capacity of isolation systems. These amplified responses propagate to the superstructure, increasing also the interstory drifts and floor accelerations [15, 16]. Therefore, the isolation system that provides the best performance for far-field GMs is not necessarily the best for near-fault GMs [17]. Furthermore, if the lateral demand exceeds the available seismic gap, the resulting impact with the moat wall can dramatically increase floor accelerations and interstory drifts [18, 19], reducing the system's efficiency [20]. Beyond lateral displacement, the vertical component of near-fault earthquakes can exceed horizontal accelerations [14, 21], which introduces a critical risk of bearing stability. These large vertical accelerations increase demands and can generate cavitation in elastomeric bearings and uplift in frictional bearings [21, 22]. This vulnerability raises the critical question of whether the performance objective of continuous operativity for Chilean BI hospitals can be reliably met under the distinct and potentially more demanding seismic hazard of crustal earthquakes generated along the SRF. Furthermore, the implications of such seismic scenarios extend beyond BI hospitals, threatening conventional fixed-base buildings and other essential infrastructure. Resulting damage could trigger widespread lifeline service disruptions and a substantial influx of patients, highlighting the essential role of hospitals in maintaining operability to support emergency medical response and manage mass casualty events.

This work evaluates the impact of crustal earthquakes along the SRF, acknowledging that its seismic potential is not negligible [6]. While the detrimental effects of near-fault GMs on isolation systems are documented in general literature, the specific vulnerability of code-compliant structures in Chile remains unquantified. The current Chilean design standard (NCh2745 [23]) assumes seismic demands derived from subduction megathrust events, potentially underestimating the pulse-like and vertical components characteristic of local crustal faults. Therefore, this study aims to quantify the reliability gap between current design provisions and the realistic hazard posed by the SRF. While such an event would affect all surrounding structures, this research focuses on the seismic performance of three critical BI hospitals with HDRBs. This paper provides the first comprehensive seismic assessment of these facilities in the context of the specific hazard that the SRF represents. The selected hospitals are located at distances between 7 and 24 km from the fault trace and provide emergency care to an extensive population. The primary challenge in this study is the significant epistemic uncertainty regarding the seismogenic capacity and source characterization of the SRF. This uncertainty includes the magnitude of the largest expected event, along with other key source parameters like corner frequency and rupture velocity. Therefore, this study has a dual aim: First, to assess the overall seismic performance of these hospitals under plausible SRF earthquake scenarios, and second, to evaluate the sensitivity of key engineering demand parameters (EDPs) to the uncertain source characteristics. To achieve these aims, physics-based synthetic earthquake simulations within a sensitivity analysis framework are used herein. A comprehensive suite of 432 GMs was generated by systematically varying these three source parameters across established bounds, as they are known to exert significant control over the resulting synthetic signals and, consequently, the demands imposed on the structures. Through this assessment, the study seeks to provide critical insights into the potential vulnerability of these healthcare facilities, thereby highlighting the need for a targeted risk assessment and, potentially, the development of appropriate mitigation strategies for the MRS.

2 | Case-Study Description

The MRS covers an approximate area of 15,403 km^2 and, according to the 2024 census, has a population of 7.4 million, representing approximately 40% of the national population [24]. Its healthcare system is organized into health services, each responsible for serving a specific geographic zone and comprising several hospitals and primary attention units. This research focuses on the seismic performance of three BI hospitals, representative of the new generation of healthcare facilities, subjected to crustal earthquake scenarios generated by the SRF, whose locations across the MRS are shown in Figure 1a. The following

10969845, 0, Downloaded from https://onlinelibrary.wiley.com/doi/10.1002/eqe.70154 by Tu Delft, Wiley Online Library on [17/03/2026]. See the Terms and Conditions (https://onlinelibrary.wiley.com/terms-and-conditions) on Wiley Online Library for rules of use; OA articles are governed by the applicable Creative Commons License

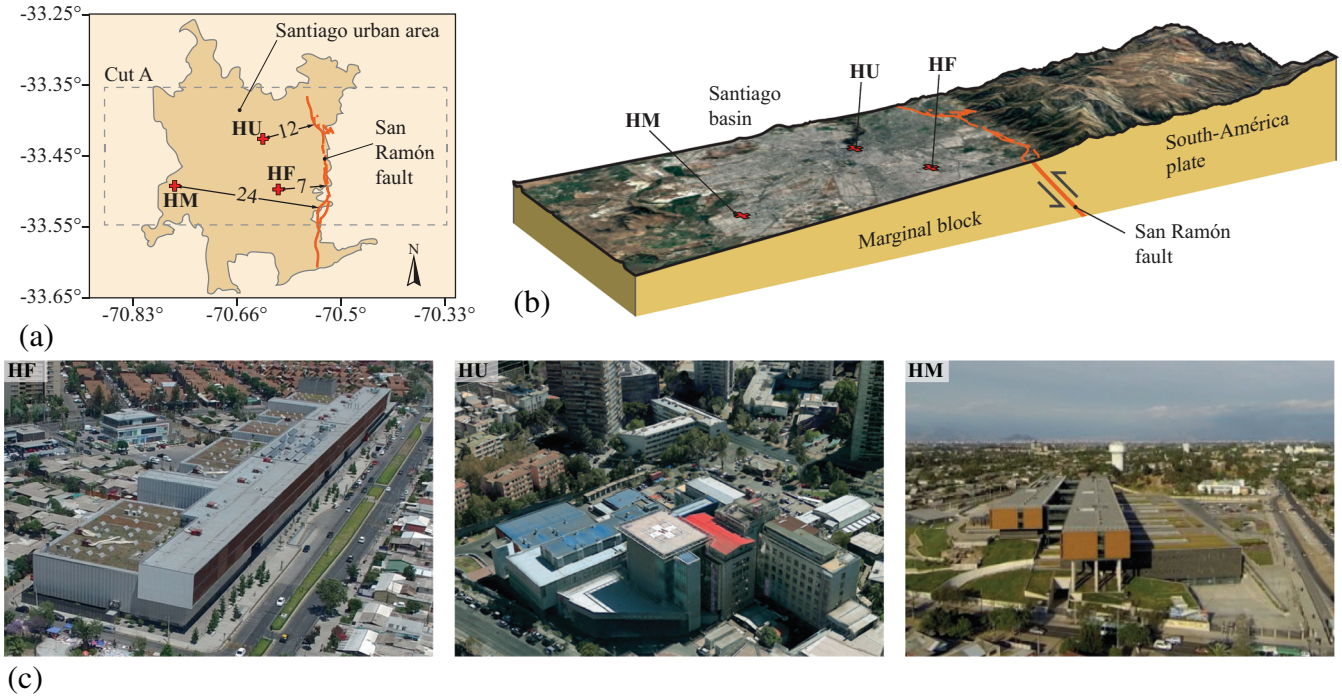


FIGURE 1 | Geographic and geological context of the SRF and the three studied BI hospitals: (a) schematic map of the MRS illustrating the surface trace of the SRF (taken from [25]) and geographic locations of the studied hospitals; (b) schematic East-West geological cross-section showing the SRF at the eastern border of the MRS and the locations of the hospitals; and (c) aerial photographs of the three BI hospitals.

subsections present detailed descriptions of the SRF and the studied BI hospitals.

2.1 | San Ramón Fault (SRF)

During the past 75 years, the boundary between the main cordillera and the central depression at the latitude of the MRS has been identified as a regional-scale fault, known as the SRF [26–29]. Early studies interpreted the SRF as a normal fault (i.e., the central depression was viewed as a downgoing block relative to the main cordillera to the east), but they did not provide detailed evidence regarding its geometry, kinematics, or seismogenic potential. More recently, Armijo et al. [6], building on earlier work by Rauld [30], provided the first refined characterization of the SRF at both local and regional scales. Through a combination of regional geology, morphological analyses, field observations of fault scarps, and detailed topographic studies, they concluded that the SRF is a west-verging reverse fault approximately 30 km in length, located at the eastern foothills of the MRS (see Figure 1a,b). Armijo et al. [6] interpreted the SRF as a surface expression of a significant structure called the West Andean Thrust, which is rooted at mid-crustal levels beneath the Andes. They estimated possible maximum earthquake magnitudes between M_w6.9 and M_w7.4. This estimate was derived from observed scarp heights of about 4 m, combined with an assumed total fault length of 30 km and a down-dip extension of approximately 15 km, along with an estimated recurrence interval of 2,500–10,000 years.

Paleoseismological studies [31] supplemented the work of Armijo et al. [6] by directly examining the faulted unconsolidated strata affected by the SRF. These studies documented two large-magnitude paleoearthquakes occurring within the last 17,000 years. The most recent event is believed to have occurred approximately 8,000 years ago and is likely to have caused surface rupture [31]. These findings imply an average slip rate of 0.45–0.64 mm/year, with a recurrence interval of approximately 9,000 years for a characteristic earthquake [9]. Later, Yañez et al. [25] studied the shallow part of the SRF (depth less than 1 km) to help develop a kinematic model that explains the deformation observed in this Andean segment. By integrating gravimetric, resistivity, seismic, and magnetic data, their research identified complex sedimentary and bedrock deformations along the SRF, including two depocenters that vary along its length. This study estimates that SRF deformation accounts for 5%–20% of Andean shortening over the last 4 million years and could generate earthquakes with magnitudes of M_w6.0–M_w6.5, with a recurrence interval of approximately 20,000 years.

Regional- and local-scale seismological surveys have shown ambiguous evidence of current seismic activity related to the projected geometry of the SRF at depth [9, 32]. Most of the shallow seismicity in this segment of the Andes is located tens of kilometers east of the SRF. In contrast, a significantly lower seismicity rate has been observed in areas that may correlate spatially with the SRF. However, the minimal seismicity associated with the SRF does not exclude the possibility that it poses a risk to the MRS, as the seismic cycle of low-slip-rate faults may impede the detection of significant seismic activity over short timeframes. To evaluate this potential hazard, Pérez-Estay et al. [9] combined three methods—stream gradient, sinuosity indexes, and gravity profiles—to estimate the potential peak

10969845, 0, Downloaded from https://onlinelibrary.wiley.com/doi/10.1002/eqe.70154 by Tu Delft, Wiley Online Library on [17/03/2026]. See the Terms and Conditions (https://onlinelibrary.wiley.com/terms-and-conditions) on Wiley Online Library for rules of use; OA articles are governed by the applicable Creative Commons License

ground acceleration (PGA) using an empirical equation. The fault was analyzed by dividing it into four segments of approximately 10 km each, which are identified as separate but not necessarily independent seismic sources. Through seismic monitoring and transient electromagnetic imaging, this work determined a dip angle of about 65° eastward and the potential for surface rupture. Results suggest that certain urban areas, especially those in hanging wall zones and fault-crossing regions, could experience horizontal PGAs exceeding 0.5 g (and locally 0.8 g) during a characteristic M_w6.2 to M_w6.7 event for the various segments of the SRF. Regardless of whether the seismic source involves individual segments or the entire fault, the SRF poses a significant risk to infrastructure due to the high PGAs that it can generate (i.e., 0.5–0.8 g on the hanging wall and 0.3–0.5 g on the footwall), much larger than the 0.2-0.3 g maximum assumed in current seismic zonation [33], which is based only on subduction earthquakes.

2.2 | Base-Isolated Hospitals

The three BI hospitals studied in this work are as follows: the La Florida Hospital (HF), the Urgent Care and Public Assistance Hospital (HU), and the Maipú Hospital (HM). These facilities were built after the 2010 Maule earthquake as part of the seismic risk mitigation plan. Figure 1a,b illustrates their geographic location relative to the SRF trace, and Figure 1c shows aerial views of the hospitals.

All structures are sited in seismic zone 2 (i.e., PGA of 0.3 g) and were designed following the Chilean design standards [23, 33] to meet the immediate occupancy performance objective, which requires the superstructure to remain elastic with interstory drifts below 0.2%. The three structures share a common structural typology, founded on isolated footings for columns and strip footings for walls: the basements comprise reinforced concrete (RC) frames and stiff perimeter shear RC walls, which behave as rigid blocks moving with the soil; the seismic isolation systems are located above the basements, and are composed of HDRBs (the HU also includes SLs), providing effective damping ratios exceeding 9.0% at design lateral displacement; and the superstructures consist of regular orthogonal grids of moment-resisting RC frames and RC floor slabs. Concrete used for basements and superstructures is of grade G25 or G30, corresponding to a nominal compressive strength (f_c') of 25 and 30 MPa, respectively. Reinforcement steel bars are of A630-420H grade, with a nominal yield stress (f_y) of 420 MPa. Further details of the three buildings and their respective isolation devices are presented in Table 1, while representative plan layouts and elevation views of the superstructures are illustrated in Figure 2.

2.2.1 | La Florida Hospital (HF)

La Florida Hospital (HF) is located in the southeast zone of the MRS. Its official name is *La Florida, Dra. Eloísa Díaz Insunza*, in honor of the first female surgeon in Chile. Inaugurated in November 2013, the building comprises a five-story structure and three basements, with an approximate plan area of 68,000 m^2. The hospital houses 403 beds and attends about 85,000 emergency cases every year (based on 2023 data [34]).

The HF is located just 7.0 km from the SRF trace (the closest of the three studied hospitals) and is founded on very stiff gravel (soil type 2). Its seismic protection system consists of 224 HDRBs, all with the same nominal properties (Table 1 provides further details). Given its proximity to the fault trace, ensuring the hospital remains fully operative is critical for providing emergency care services and managing the potential surge of casualties from surrounding areas in the aftermath of an earthquake.

2.2.2 | Urgent Care and Public Assistance Hospital (HU)

The Urgent Care and Public Assistance Hospital (HU) is located in a central downtown area of the MRS. Its origins date back to August 7, 1911, with the establishment of the first permanent and formal urgent care service. At the time, the police headquarters hired medical students to provide emergency healthcare in the area, which led to the service being named *Asistencia Pública* (public assistance) for the injured, this name was updated to the current one in 1994. More recently, between 2013 and 2014, a new seismically isolated structure was built, funded by donations from Catholic Bishop Sergio Valech. This new building comprises three stories above ground and two basements, with a total plan area of approximately 8,000 m^2. In terms of capacity, the hospital houses 294 beds and attends about 125,000 emergency cases every year (based on 2023 data [35]).

The HU is located 12.0 km from the SRF trace and is founded on very stiff gravel (soil type 2). Its seismic isolation system is hybrid, composed of 33 HDRBs (Table 1 provides further details) and 19 SLs. The SLs have diameters of 35 and 45 cm with a total height of 28 cm. Their nominal friction coefficient, at velocities exceeding 15 cm/s, ranges between 5% and 7%, while their maximum axial stress is 15 or 22 MPa for the long- and short-term loads, respectively. This facility is in the heart of downtown Santiago and is surrounded by many old buildings, potentially seismically vulnerable (such as masonry buildings in the Yungay neighborhood), which could contribute to a significant surge of patients after an earthquake scenario.

2.2.3 | Maipú Hospital (HM)

The Maipú Hospital (HM) is located in the southwest zone of the MRS. The current structure was inaugurated in December 2013, and its official name is *El Carmen, Dr. Luis Valentín Ferrada Urzúa*, honoring a beloved physician known as the *people's doctor*. The structure comprises seven stories above ground and one basement, with a total plan area of approximately 70,000 m^2. In terms of capacity, the hospital has 439 beds and attends about 125,000 emergency cases every year (based on 2023 data [36]).

The HM is located at 24 km from the SRF trace (the furthest of the three studied hospitals) and is founded on soil classified as type 3 (sand or gravel). Its seismic isolation system is composed of 278 HDRBs, divided into two nominal designs to accommodate different axial loads (Table 1 provides further details). Its location

10969845, 0, Downloaded from https://onlinelibrary.wiley.com/doi/10.1002/eqe.70154 by Tu Delft, Wiley Online Library on [17/03/2026]. See the Terms and Conditions (https://onlinelibrary.wiley.com/terms-and-conditions) on Wiley Online Library for rules of use; OA articles are governed by the applicable Creative Commons License

TABLE 1 | Characteristics of the three BI hospitals.

Property	Hospital		
	HF	**HU**	**HM**
Location			
Latitude	33°30′51.18″ S	33°26′38.93″ S	33°30′51.16″ S
Longitude	70°35′54.65″ W	70°38′17.49″ W	70°45′54.36″ W
Distance from the SRF, d_{SRF} [km]	7.0	12.0	24.0
Site characteristics			
Seismic zone	II	II	II
Soil type	2 (very stiff gravel)	2 (very stiff gravel)	3 (sand or gravel)
Structure			
Year of completion	2013	2014	2013
Number of stories and basements, N and N_b	5+3	3+2	7+1
Plan dimensions, $L_x \times L_y$ [m]	300.0×41.5	47.8×52.2	172.5×77.0
Total plan area, A_t [m^2]	68,000	8,000	70,000
Seismic weight, W [kN]	711,836	86,156	724,230
Isolation system	224 HDRB	33 HDRB+19 SL	278 HDRB =212+(66)[a]
HDRB properties			
External diameter, D_e [mm]	750	650	700 (850)[a]
Internal diameter, D_i [mm]	150	100	100 (150)[a]
Steel plate thickness, t_s [mm]	3	3	3 (3)[a]
Rubber layer thickness, t_r [mm]	6	7	6 (6)[a]
Number of rubber layers, n_r [—]	28	21	34 (34)[a]
Total height, H_t [mm]	289	247	343 (343)[a]
Shear stiffness rubber, G_r [kgf/cm^2]	5.0	4.0	5.0
Design lateral displacement, u_{des} [cm]	21.42 [21.99][b]	18.90 [19.70][b]	23.90 [24.10][b]
MCE max. lateral displacement, u_{mce} [cm]	26.75 [27.47][b]	23.90 [24.90][b]	31.20 [31.70][b]
Average shear strain at the MCE, $\gamma_{mce} = u_{mce}/(t_r n_r)$ [%]	159.2	162.6	152.9

Note: Data include geographic location, site and soil characteristics, general structural features, type and configuration of their isolation systems, and specific geometric and mechanical properties for the HDRBs.

Abbreviations: HDRB, high damping rubber bearing; SL, frictional sliders.

[a]Value between parentheses corresponds to second type of isolator.

[b]Value between brackets includes torsional effects.

on the opposite side of the city from the SRF trace, positions it to play a crucial role in the post-earthquake response by managing noncritical patients or serving as a backup facility if hospitals closer to the fault are compromised.

3 | Numerical Modeling

This section details the numerical modeling framework used to evaluate the seismic performance of the three BI hospitals under potential SRF earthquakes and the sensitivity of their response to key seismic source parameters. This framework integrates two components as follows: physics-based earthquake simulations to generate GM at the hospital locations—a necessary approach given the lack of reliable empirical data from the SRF—and detailed three-dimensional (3D) nonlinear finite element (FE) models of the hospitals developed using the OpenSees software [37].

3.1 | Earthquake Rupture Model and Ground Motion Modeling

The GM time-series at each hospital foundation was generated using the UCSB method [38]. This approach provides realistic earthquake rupture scenarios by addressing the computational challenges of dynamic rupture modeling while maintaining physical realism through careful calibration against physics-based simulations [39]. Figure 3 presents a flowchart illustrating this methodology, including the generation of the rupture scenarios and the wave propagation to the hospital locations. Notice that this systematic approach ensures that

10969845, 0, Downloaded from https://onlinelibrary.wiley.com/doi/10.1002/eqe.70154 by Tu Delft, Wiley Online Library on [17/03/2026]. See the Terms and Conditions (https://onlinelibrary.wiley.com/terms-and-conditions) on Wiley Online Library for rules of use; OA articles are governed by the applicable Creative Commons License

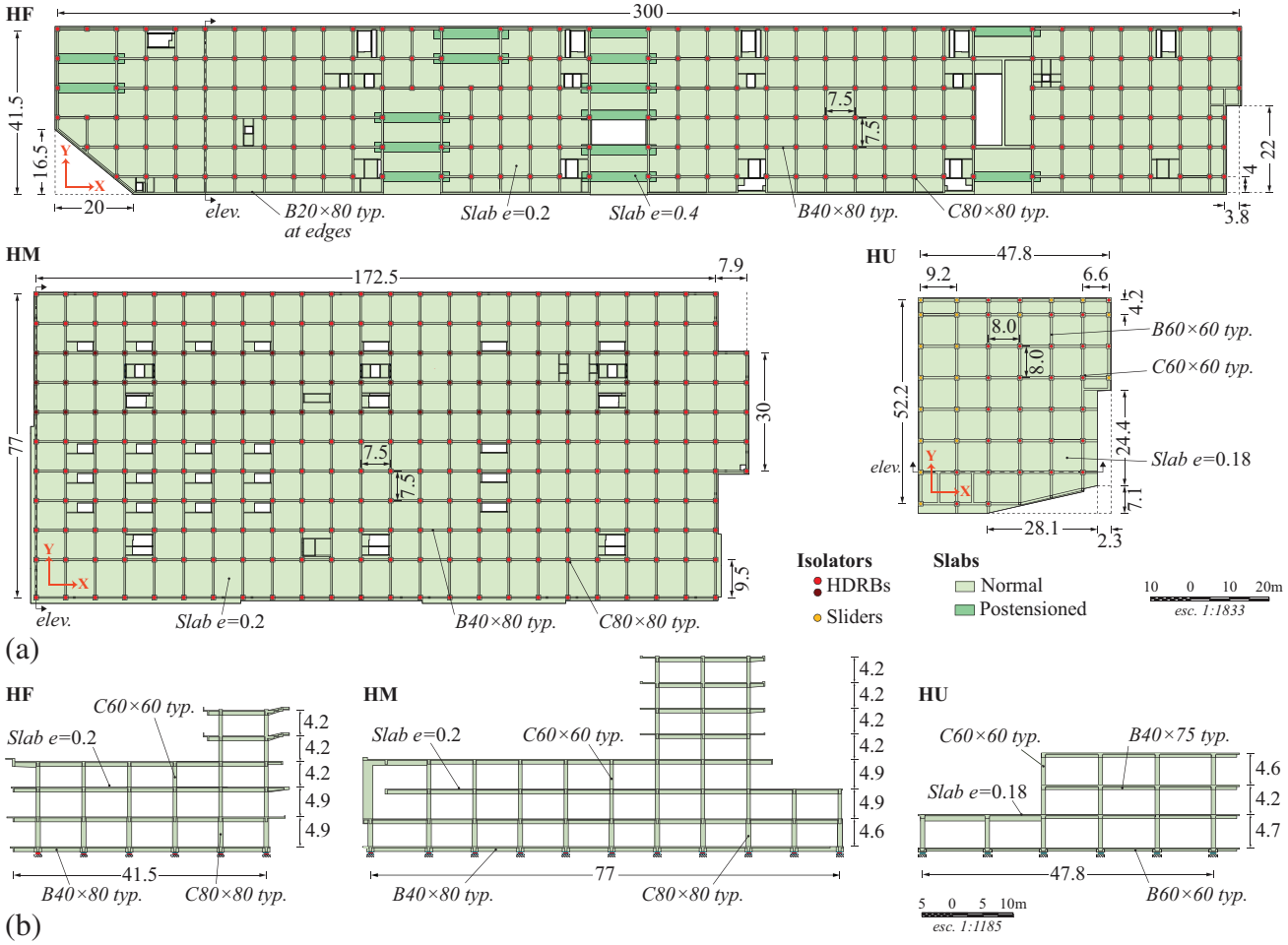


FIGURE 2 | Structural layouts of the three studied hospitals: (a) plan views at the isolation system level, including the general building and structural element dimensions, and arrangement of HDRBs (different red tones represent devices with different geometric characteristics) and SLs, and (b) representative elevations showing story heights and frame configurations. The *Y*-direction of all three hospitals aligns closely with the north-south direction, parallel to the fault trace.

the simulations capture the features inherent to near-fault motions, including long-period velocity pulses and large vertical accelerations.

3.1.1 | Earthquake Rupture

The calculation of GM from fault slip is governed by the representation theorem [40], which relates these two physical quantities through the following integral equation:

$$u_n(\mathbf{x},t)=\int_{-\infty}^{\infty}d\tau\iint_{\Sigma}s_i(\boldsymbol{\xi},\tau)c_{ijpq}m_jG_{np,q}(\mathbf{x},t-\tau;\boldsymbol{\xi},0)\,d\Sigma, \quad (1)$$

where $u_n(\mathbf{x},t)$ is the n-th component of ground displacement at position $\mathbf{x}$ and time t, $s_i(\boldsymbol{\xi},\tau)$ is the i-th component of the slip on fault plane Σ at position $\boldsymbol{\xi}$ and time τ, c_{ijpq} are the coefficients of the elasticity tensor, m_j is the j-th component of the fault normal, and $G_{np,q}$ is the spatial derivative of the Green's function. The kinematic source model proposed by Haskell [41] was the first to apply this framework by prescribing the activation of slip on each point on the fault plane.

The temporal evolution of slip is defined by a three-phase slip-rate function that resembles the Kostrov slip-rate:

$$\dot{s}(t)=\begin{cases}\frac{At}{T_p}\sqrt{\frac{a+b}{T_p^2}}\sin\left(\frac{\pi t}{2T_p}\right) & 0\le t<T_p\\ A\sqrt{\frac{a+b}{t^2}} & T_p\le t<0.7T_r\\ A\sqrt{\frac{a+b}{t^2}}\sin\left(\frac{5\pi(T_r-t)}{3T_r}\right) & 0.7T_r\le t<T_r\end{cases}, \quad (2)$$

where T_r is the rise-time, T_p is the peak-time, A is a normalization constant, and the coefficients $a=1$ and $b=100$ are calibrated to produce the desired ω^{-2} spectral characteristics. To ensure physical realism, the statistical properties of the rupture parameters are carefully prescribed using physics-derived distributions from over 300 dynamic rupture simulations [42]. Final slip follows a truncated Cauchy distribution with mean slip $\bar{s}=M_0/\mu A_r$, where M_0 is the seismic moment, μ is the shear modulus, and A_r is the rupture area. Rise-time (T_r) is drawn from a Beta distribution over the interval 0.2–1.0 s; peak-time (T_p) follows a Beta distribution as a fraction of the rise-time; and rupture velocity (V_r) is characterized by a Lévy distribution (stability

10969845, 0, Downloaded from https://onlinelibrary.wiley.com/doi/10.1002/eqe.70154 by Tu Delft, Wiley Online Library on [17/03/2026]. See the Terms and Conditions (https://onlinelibrary.wiley.com/terms-and-conditions) on Wiley Online Library for rules of use; OA articles are governed by the applicable Creative Commons License

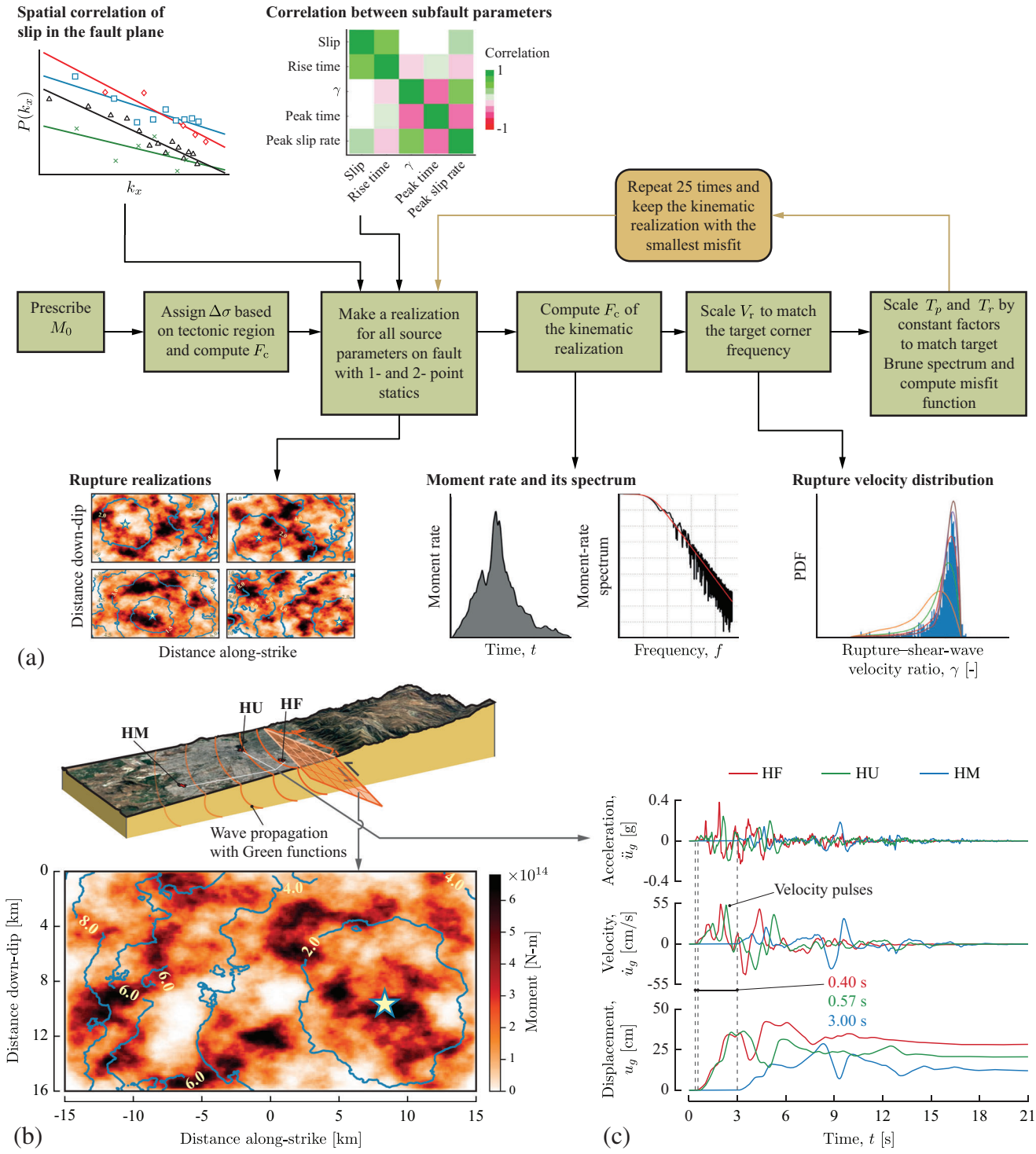


FIGURE 3 | Ground motion simulation method: (a) flowchart of the procedure for the generation of the earthquake rupture scenarios; (b) wave propagation to the hospital locations; and (c) representative GM time-series with velocity pulses (M_W 6.5, V_r = 3.0 m/s, F_c = 0.09 Hz).

parameter, $\alpha = 1.14$; skewness, $\beta = 0.99$; scale, $\sigma = 0.035$; and location, $\nu = 0.84$). Spatial correlations between rupture parameters are implemented using von Kármán power spectrum applied in the wavenumber domain using the following:

$$F(k_x, k_y) = \frac{1}{1 + (C_L k_x)^2 + (C_W k_y)^2}, \tag{3}$$

where C_L and C_W are the correlation lengths along strike and dip, respectively, which are typically assumed as equal ($C_L = C_W$) and scale with magnitude [39], depending on the target earthquake magnitude and regional characteristics. The method maintains correlations between different source parameters using the NORTA (NORmal-To-Anything) algorithm [43], ensuring that relationships derived from dynamic rupture simulations are preserved, such as the near-zero correlation

10969845, 0, Downloaded from https://onlinelibrary.wiley.com/doi/10.1002/eqe.70154 by Tu Delft, Wiley Online Library on [17/03/2026]. See the Terms and Conditions (https://onlinelibrary.wiley.com/terms-and-conditions) on Wiley Online Library for rules of use; OA articles are governed by the applicable Creative Commons License

between slip and normalized rupture velocity. Finally, the corner frequency (F_c) is determined from the target stress drop:

$$F_c = \frac{1}{2\pi}\sqrt{\frac{7M_0}{16\rho\beta^3 r^3}}, \quad (4)$$

with stress drops in this study typically ranging from 5.24 to 10.8 MPa.

The implementation begins by generating correlated white noise for each parameter, followed by spatial filtering in the wavenumber domain with von Kármán filters. The rise-time and peak-time are then linearly scaled to achieve both the target seismic moment (M_0) and the desired ω^{-2} moment-rate spectrum characteristics.

3.1.2 | Ground Motion Simulation

Green's functions were computed using the discrete frequency-wavenumber method [44] for a layered 1D velocity structure. The final synthetic seismograms for each hospital were then produced by applying the representation theorem, convolving the slip-rate functions with the corresponding Green's functions and summing the contributions from all sub-faults.

The simulations were conducted within a parametric framework to account for the significant epistemic uncertainties in the SRF's seismogenic capacity. Three source parameters were systematically varied as follows: three moment magnitudes, M_w, were considered—scenarios of 6.5, 6.9, and 7.2— based on the range of possible maximum magnitudes for the SRF identified in the literature (Section 2.1); average rupture velocities, V_r, of 2.5, 3.0, and 3.5 km/s were used for all magnitudes, consistent with inferred rupture speeds from copious amounts of earthquakes; and corner frequencies of the moment-rate spectra, F_c, were selected to be consistent with the magnitudes, as proposed by Aki [45]: 0.12, 0.14, and 0.16 Hz for M_w6.5; 0.07, 0.09, and 0.11 Hz for M_w6.9; and 0.05, 0.07, and 0.09 Hz for M_w7.2.

Since the UCSB method simulates GM from finite faults, a fault geometry and rupture area must be defined for each rupture scenario. These were determined using the self-consistent earthquake fault scaling relationships established by Leonard [46]. These relationships link rupture area, length, width, and average displacement to the moment magnitude ($\log_{10}(A_r) = M_w - 4.0$, with A_r in km^2), ensuring consistency with the fundamental seismic moment equation $M_0 = \mu A_r D$, where D is the fault displacement. For reverse faults like the SRF, these laws predict a dramatic increase in rupture size with magnitude; for example, M_w7.0 event involves a rupture area approximately 10 times larger than a M_w6.0 event.

The parametric approach resulted in a total of 27 unique earthquake scenarios (see Table 2). To account for between-event variability, 16 realizations were generated for each scenario, yielding a suite of 432 synthetic GM records.

Figure 3c presents representative GM time-series for an M_w6.9 scenario, with V_r of 3.0 km/s and F_c of 0.09 Hz. The moment distribution across the rupture plane is nonuniform, with a randomly located hypocenter, as expected in actual earthquakes (Figure 3b). The resulting acceleration time-series (see Figure 3c) shows realistic characteristics: PGA attenuates with distance from the fault, seismic wave arrival times vary according to each hospital's location, and long-period velocity pulses.

TABLE 2 | Earthquake scenarios considered in the analyses with variable moment magnitude, M_W, rupture velocity, V_r, in km/s, and corner frequency, F_c, in Hertz.

Scenario number	M_W	V_r [km/s]	F_c [Hz]
1	6.5	2.5	0.12
2	6.5	2.5	0.14
3	6.5	2.5	0.16
4	6.5	3.0	0.12
5	6.5	3.0	0.14
6	6.5	3.0	0.16
7	6.5	3.5	0.12
8	6.5	3.5	0.14
9	6.5	3.5	0.16
10	6.9	2.5	0.07
11	6.9	2.5	0.09
12	6.9	2.5	0.11
13	6.9	3.0	0.07
14	6.9	3.0	0.09
15	6.9	3.0	0.11
16	6.9	3.5	0.07
17	6.9	3.5	0.09
18	6.9	3.5	0.11
19	7.2	2.5	0.05
20	7.2	2.5	0.07
21	7.2	2.5	0.09
22	7.2	3.0	0.05
23	7.2	3.0	0.07
24	7.2	3.0	0.09
25	7.2	3.5	0.05
26	7.2	3.5	0.07
27	7.2	3.5	0.09

3.2 | Structures

3D nonlinear FE models of the three BI hospitals were developed in OpenSees [37]. The numerical models originally developed in ETABS by the structural engineering consultants for the design of these hospitals were used as a benchmark (some differences with the actual as-built structures could exist); all nodes, elements, connectivity, and elastic mechanical properties were translated to OpenSees to develop the final nonlinear models. The models

10969845, 0, Downloaded from https://onlinelibrary.wiley.com/doi/10.1002/eqe.70154 by Tu Delft, Wiley Online Library on [17/03/2026]. See the Terms and Conditions (https://onlinelibrary.wiley.com/terms-and-conditions) on Wiley Online Library for rules of use; OA articles are governed by the applicable Creative Commons License

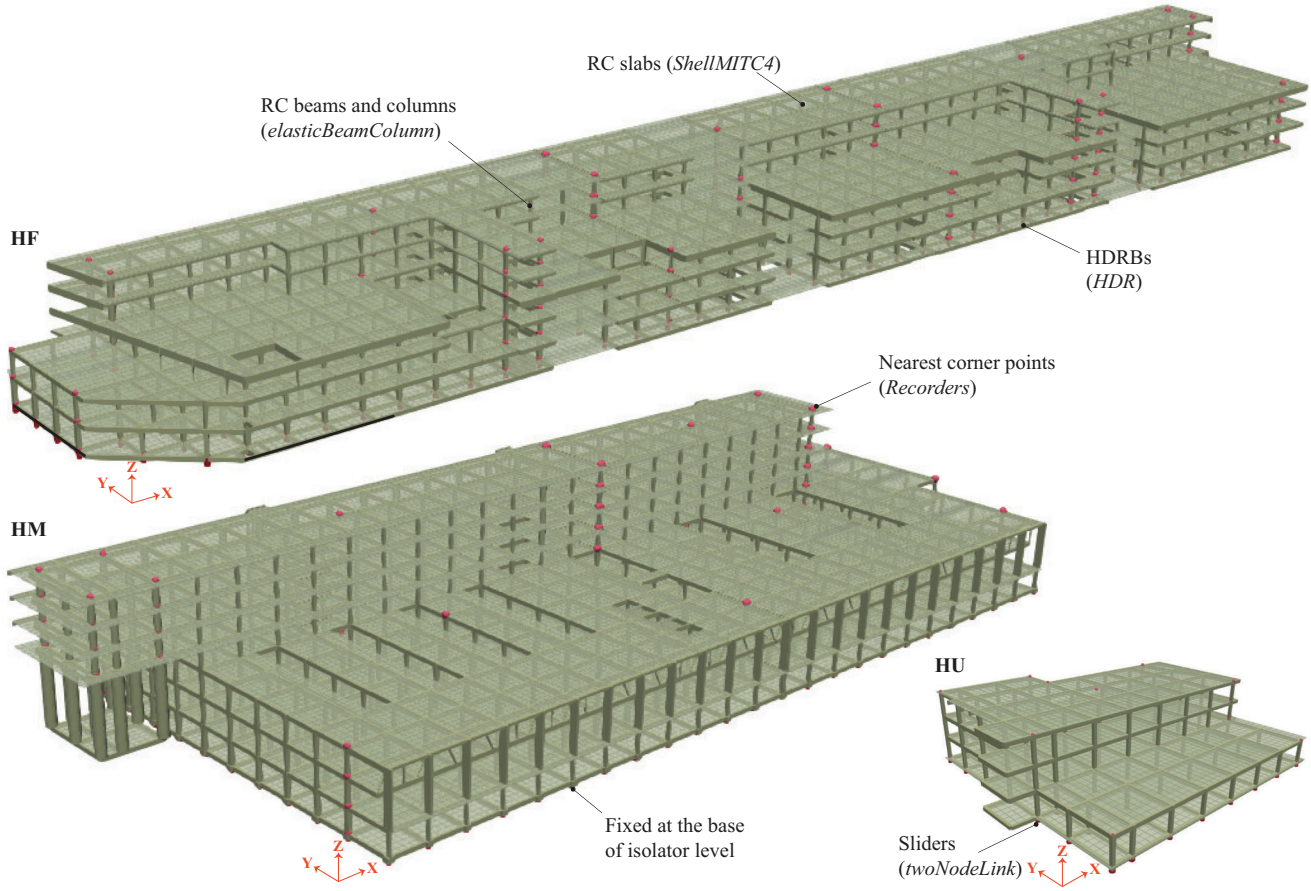


FIGURE 4 | 3D FE models of the three BI hospitals developed in OpenSees: HF on the top, HM on the bottom left, and HU on the bottom right. The models include the isolation system (HDRBs and SLs) and the superstructure (slabs, beams, and columns), indicating modeling assumptions and the used OpenSees element types (i.e., *ShellMITC4* for slabs, *elasticBeamColumn* for frames, *HDR* for HDRBs and *TwoNodeLink* for SLs). These models were visualized in ParaView, using a Python module developed by the authors.

include all structural elements of the seismic isolation system and superstructure. Conversely, the substructures (basements) were assumed to behave rigidly and were excluded from the numerical model, given that they are buried in the ground and have large, thick perimeter shear walls. The main modeling assumptions are fixity at the base of the isolation layer, and seismic mass computed as the self-weight plus 50% of the live loads. This mass is distributed to the nodes based on tributary areas and applied as lumped nodal mass. Figure 4 presents the FE models, detailing the main assumptions and element types, while Tables 3 and 4 summarize the material properties for the superstructures and isolation devices, respectively.

The numerical models assumed a linear-elastic behavior for all elements in the superstructure, as generally expected in BI buildings. Therefore, the mechanical properties assigned to the RC elements were a mass density (ρ_c) of 2.50 ton/m^3, a Poisson's ratio (ν_c) of 0.2, and dynamic Young's modulus (E_{dyn}) computed as $E_{\text{dyn}} = 12.81\,(\rho_c E_{\text{sta}})^{5/7}$ [47], with ρ_c in ton/m^3 and $E_{\text{sta}} = 4700\sqrt{f_c'}$ with f_c' in MPa [48]. RC beams and columns were modeled using two-node frame elements (*elasticBeamColumn*), while slabs were represented using four-node shell elements (*ShellMITC4*) with an isotropic section (*ElasticMembranePlateSection*). A compatible mesh between all structural elements was developed with a maximum element size of 1.5 m. HDRBs were modeled using a two-node bearing element (*HDR*). This element incorporates the hysteretic model proposed by Grant et al. [49] for the shear response, the cavitation model proposed by Kumar et al. [50] for tensile loads, and a simplified version of the two-spring model [51] for axial-shear coupling. The remaining degrees of freedom (bending and torsion) were considered linear-elastic and uncoupled, and characterized by stiffness values computed according to the formulations presented by Kelly and Konstantinidis [52]. SLs were modeled using two-node link elements (*twoNodeLink*). While these are friction-based devices, they were represented using an effective linear stiffness (elastic material) calibrated to their behavior at the design displacement (calibrated from experimental data). This simplification was necessary to ensure numerical convergence across all seismic scenarios in which large vertical accelerations induced uplift (see Section 5 for further discussion). To assess performance, key EDPs were recorded at the center of mass and corners of each floor. These included the nodal displacements, velocities, and absolute accelerations. For the isolation devices, local displacements and forces were recorded for all degrees of freedom.

The parameters for simulating the shear response of the HDRBs for all three hospitals were calibrated to match the experimental results of quality control tests (also called production tests in

10969845, 0, Downloaded from https://onlinelibrary.wiley.com/doi/10.1002/eqe.70154 by Tu Delft, Wiley Online Library on [17/03/2026]. See the Terms and Conditions (https://onlinelibrary.wiley.com/terms-and-conditions) on Wiley Online Library for rules of use; OA articles are governed by the applicable Creative Commons License

TABLE 3 | Summary of modeling assumptions, OpenSees element types, and property values for the superstructures.

Component	Hospital		
	HF	**HU**	**HM**
Beams and columns			
Element		*elasticBeamColumn*	
Young's modulus, E_{dyn} [MPa]	25,743	23,500	25,743
Shear modulus, G_c [MPa]	10,726	9,792	10,726
Mass density, ρ_c [ton/m^3]	2.50	2.50	2.50
Slabs			
Element		*ShellMITC4*	
Section		*ElasticMembranePlateSection*	
Young's modulus, E_{dyn} [MPa]	25,743	23,500	25,743
Poisson's ratio, ν_c [—]	0.20	0.20	0.20
Mass density, ρ_c [ton/m^3]	2.50	2.50	2.50
Damping			
Model		Rayleigh	
Damping coefficient (mass), β_m [—]	0.0	0.0	0.0
Damping coefficient (stiffness), β_s [—]	0.0070	0.0046	0.0083

TABLE 4 | Parameters for the *HDR* element used for the case-study hospital models.

Parameter	Unit	Hospital			
		HF	**HU**	**HM**	
		H5D75	**H4D65**	**H5D70**	**H5D85**
Rubber					
G_r	MPa	0.4905	0.3923	0.4905	0.4905
K_{bulk}	MPa	2000	2000	2000	2000
Shear response[a]					
a_1	—	1348.0095	1024.2079	830.8551	1442.7628
a_2	—	-3.6561×10^{-3}	-4.7210×10^{-3}	-1.7994×10^{-3}	-5.2385×10^{-3}
a_3	—	1.7752×10^{-7}	1.5395×10^{-7}	7.6116×10^{-8}	1.1738×10^{-7}
b_1	—	44352.3830	37627.9980	39204.8690	67571.2340
b_2	—	0.4189	0.1834	4.6551×10^{-2}	0.2564
b_3	—	7.7821×10^{-2}	7.8335×10^{-2}	5.7930×10^{-2}	6.1301×10^{-2}
c_1	—	1.7581×10^{-8}	1.9299×10^{-8}	1.2186×10^{-8}	1.3319×10^{-8}
c_2	—	1.5645×10^{-7}	8.3353×10^{-8}	1.3943×10^{-7}	1.0048×10^{-7}
c_3	—	0.8471	0.8781	1.0450	0.9524
c_4	—	5.0242×10^{-11}	1.2651×10^{-11}	9.8012×10^{-12}	3.5354×10^{-11}
Cavitation					
k_c	—	10.0	10.0	10.0	10.0
ϕ_M	—	0.1	0.1	0.1	0.1
a_c	—	1.0	1.0	1.0	1.0

[a]Units of all parameters must be consistent.

10969845, 0, Downloaded from https://onlinelibrary.wiley.com/doi/10.1002/eqe.70154 by Tu Delft, Wiley Online Library on [17/03/2026]. See the Terms and Conditions (https://onlinelibrary.wiley.com/terms-and-conditions) on Wiley Online Library for rules of use; OA articles are governed by the applicable Creative Commons License

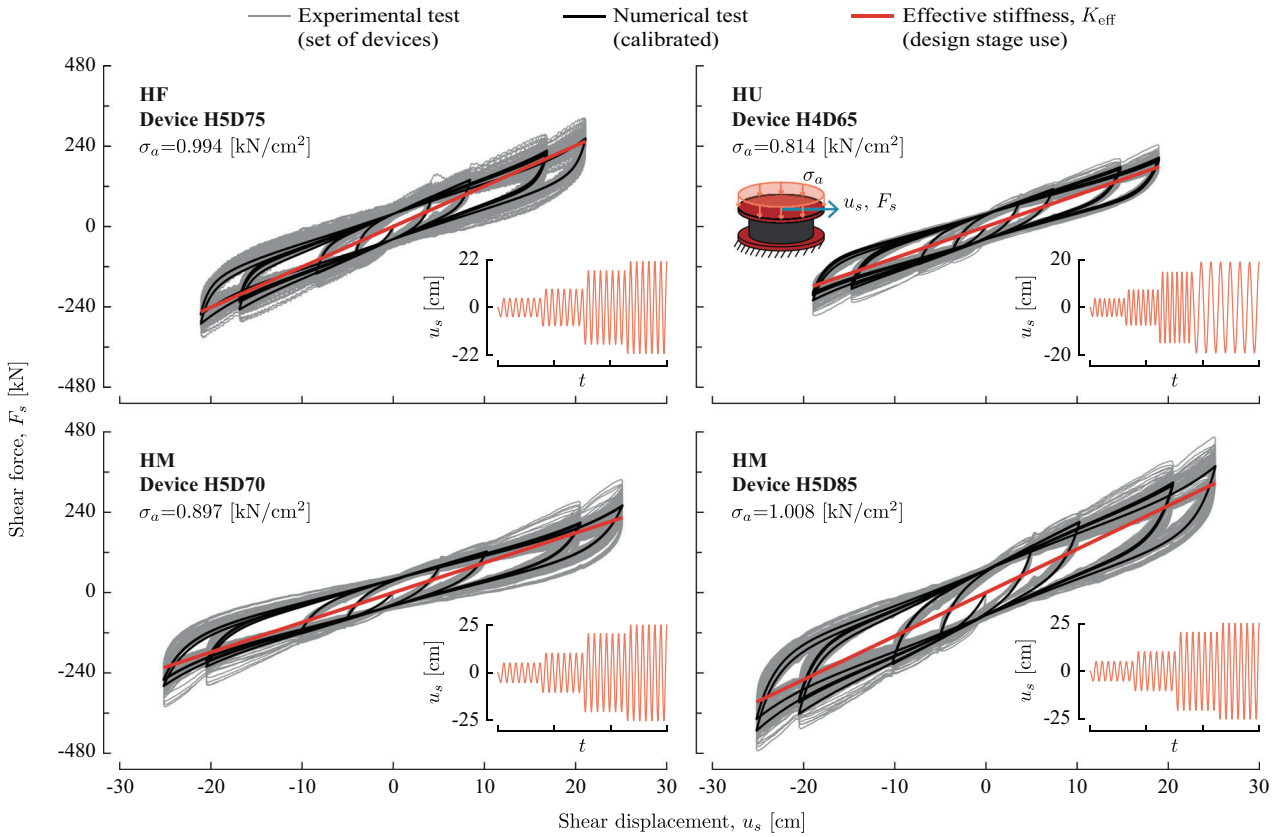


FIGURE 5 | Comparison between experimental and calibrated numerical shear force–displacement ($F_s(u_s)$) hysteresis for HDRBs from the three hospitals at the indicated compressive axial stress (σ_a). Each subplot shows multiple experimental test results (gray lines) for nominally identical devices alongside the numerical response (black line) obtained using the parameters calibrated to represent the average behavior of the device batch and the computed effective stiffness, K_{eff} (red line).

the ASCE7 [53]) performed on the devices used in the actual hospitals. These experimental results are part of the database presented by Miranda et al. [54]. The isolation devices were subjected to consecutive sequences of cyclic lateral deformation under constant axial load. Given the inherent aleatory uncertainty in the mechanical behavior of nominally identical devices (see Figure 5), the response of a device with an average behavior from each batch was chosen for the model calibration. This calibration process was automated by using the covariance matrix adaptation evolution strategy (CMA-ES) algorithm [55, 56] to minimize the mean squared error between the measured and numerical shear forces for each sampled deformation, as defined by the following:

$$\hat{\theta} = \text{argmin}_{\theta}\left(\frac{1}{m}\sum_{j=1}^{m}\left(F_{s,j} - \hat{F}_{s,j}(\theta)\right)^2\right), \tag{5}$$

where θ is the vector with the model parameters and $\hat{\theta}$ its estimates, m is the number of sampled points, $F_{s,j}$ is the measured shear force at the jth sampled deformation $\left(u_{s,j}\right)$, and $\hat{F}_{s,j}(\theta)$ is the force estimate by the numerical model using the parameters θ.

Figure 5 compares the shear force–displacement ($F_s(u_s)$) hysteresis of the calibrated numerical model against the experimental results, showing a close match with the average behavior of the device batch. A summary of the calibrated parameter values for the HDRBs in all three hospitals is presented in Table 4. This approach aims to provide estimates of the seismic response of the entire isolation system that are representative of its likely actual behavior.

Energy dissipation due to minor inelasticity and interactions with nonstructural components was accounted for using Rayleigh's damping model. The damping matrix of the superstructure was assembled neglecting the contribution of the mass component to avoid damping leakage [57, 58]. A critical damping ratio of 2% at the natural vibration frequency of the fixed-base superstructure was selected. Consequently, the *region* command was used to apply this damping exclusively to the superstructure elements, ensuring that it does not superimpose with the explicitly modeled energy dissipation of the isolation layer (last rows of Table 3 presents the values of the Rayleigh's coefficients).

While the initial tangent stiffness of elements could be used for evaluating the modal periods in some nonlinear models (this approach is used by OpenSees), it could lead to nonrepresentative results for structures with HDRBs. Therefore, to accurately assess the modal periods of the hospital models, the effective shear stiffness (K_{eff}) of the HDRBs was used. This stiffness was derived from the quality control test data. First, for each device tested within a batch the K_{eff} for the first three deformation cycles at the design displacement amplitude was computed as $K_{\text{eff}} = (|F_s^+| +$

10969845, 0, Downloaded from https://onlinelibrary.wiley.com/doi/10.1002/eqe.70154 by Tu Delft, Wiley Online Library on [17/03/2026]. See the Terms and Conditions (https://onlinelibrary.wiley.com/terms-and-conditions) on Wiley Online Library for rules of use; OA articles are governed by the applicable Creative Commons License

TABLE 5 | Comparison of the first three vibration periods (in seconds) and their predominant directions obtained from the ETABS design models and the developed OpenSees models for the three BI hospitals.

Mode	ETABS	OpenSees	Diff. [%]
HF			
1	3.3558 (Y)	3.3890 (Y)	0.99
2	3.3320 (X)	3.3772 (X)	1.36
3	3.2454 (Θ)	3.2770 (Θ)	0.97
HU			
1	3.1501 (X)	3.1386 (X)	0.37
2	3.1456 (Y)	3.1351 (Y)	0.33
3	2.9302 (Θ)	2.9229 (Θ)	0.25
HM			
1	3.3481 (X)	3.4146 (X)	1.99
2	3.3324 (Y)	3.3975 (Y)	1.95
3	3.2139 (Θ)	3.2797 (Θ)	2.05

Note: See Figure 4 for the definition of the reference axes.

$|F_s^-|)/(|u_s^+| + |u_s^-|)$ [53], where $F_s^{\pm}$ are the positive and negative shear force at the respective positive and negative maximum displacements $u_s^{\pm}$. Second, the mean of these first three cycles was used to define the effective stiffness of that individual device. Finally, the effective stiffness for each HDRB type was computed by averaging the values from all devices within that type. Figure 5 provides a graphical interpretation of this effective stiffness. The approach is validated by the results in Table 5, which compares the first three vibration periods for all hospital models between ETABS and OpenSees, showing only negligible differences ($\leq$ 2.05%).

4 | Results

This section presents the seismic performance assessment of the three BI hospitals when subjected to earthquakes generated by the SRF. The analysis presented here focuses on the nine scenarios corresponding to an M_w 6.9 earthquake. Each scenario is derived from combinations of three corner frequencies (F_c) and three rupture velocities (V_r), and includes 16 realizations per scenario to account for between-event variability (see Table 2 for the full list of scenarios). Due to space constraints, the results of the other 18 scenarios corresponding to M_w6.5 and M_w7.2 earthquakes are provided as Supporting Material. First, the seismic hazard at the hospital locations is quantified for each scenario and compared against the current Chilean design spectra. Then, the detailed results from the nonlinear response history analyses of the three BI hospitals are presented, focusing on EDPs used for assessing structural performance.

4.1 | Seismic Hazard of the SRF

The earthquake simulations produced GM time-series at the location of each studied BI hospital. Given the varying distances of these healthcare facilities from the SRF trace, significant differences in the intensity and frequency content of the GMs—and thus hazard levels—are expected. Although this study focuses on the impact of the SRF on BI hospitals, these data also provide valuable insights into the potential seismic demands on surrounding structures, thereby identifying potential areas for future research and broader risk assessment in the MRS.

Figure 6 presents the vertical ($Sa_V(T)$) and horizontal RotD100 ($Sa_H(T)$) pseudo-acceleration spectra with a critical damping ratio of 5% of all nine scenarios corresponding to an earthquake magnitude of M_w6.9 at the locations of the (see Figures S1 and S2 for M_w6.5 and M_w7.2, respectively). RotD100 refers to the maximum horizontal spectral acceleration obtained when considering all possible nonredundant orientations of the two horizontal components of the recorded GM [59]. Each plot represents one seismic scenario and includes the response spectra from all 16 realizations at each hospital location, the mean spectrum of the seismic scenario, and the design spectrum specified by the current Chilean design standard [23] (note that the vertical design spectrum is defined as two-thirds of the horizontal design spectrum), along with the typical range of vertical vibration periods for HDRBs and the fundamental horizontal translational periods of the hospitals. A visual inspection of the spectra reveals clear trends in the data. As expected, the spectra for the HM generally show the lowest spectral values due to its larger distance from the fault trace. Conversely, the spectra for the HF show the largest demands, though with some exceptions relative to the HU location for specific period intervals and source parameter combinations. The source parameters also have a strong influence: increasing the V_r while keeping the F_c constant results in larger spectral values across all periods; when V_r is kept constant, an increase in the F_c tends to raise the spectral demands for short periods (below 1.0 s). Comparison of the mean spectra against the design spectra shows that the demands for the farthest hospital (HM) tend to be lower than those considered during the design stage, except for scenarios with upper-bound values of V_r and F_c in the vertical direction. However, the opposite is observed for the other two hospitals (HF and HU), whose demands exceed those specified by the design spectrum in most scenarios. This exceedance is particularly significant around the first vibration period of the buildings in the horizontal direction and for short periods (typical for HDRBs) in the vertical direction. Indeed, only the scenario with the lowest corner frequency (F_c = 0.07 Hz) combined with the lowest rupture velocity (V_r = 2.5 km/s) results in demands that do not exceed those considered by the design spectrum.

Table 6 presents three commonly used intensity measures (IMs) computed from the mean horizontal response spectra ($Sa_H(T)$) for all nine seismic scenarios, alongside the corresponding values from the design spectra. These IMs are as follows: (i) the PGA_H; (ii) spectral displacement at the first vibration period of the structure ($Sd_H(T_1)$); and (iii) spectral acceleration at the first vibration period ($Sa_H(T_1)$), where T_1 represents the fundamental isolated period of the respective hospital. These values confirm the trends observed in Figure 6, where increasing V_r or F_c tends to increase the demands. At the location of the HF, the closest to the SRF trace (7.0 km), PGAs could be up to three times the value of the design code. Regarding $Sd_H(T_1)$ and $Sa_H(T_1)$, M_w 6.9 scenarios provide demands up to 80% larger than those specified for design. For the HU, located at an intermediate

10969845, 0, Downloaded from https://onlinelibrary.wiley.com/doi/10.1002/eqe.70154 by Tu Delft, Wiley Online Library on [17/03/2026]. See the Terms and Conditions (https://onlinelibrary.wiley.com/terms-and-conditions) on Wiley Online Library for rules of use; OA articles are governed by the applicable Creative Commons License

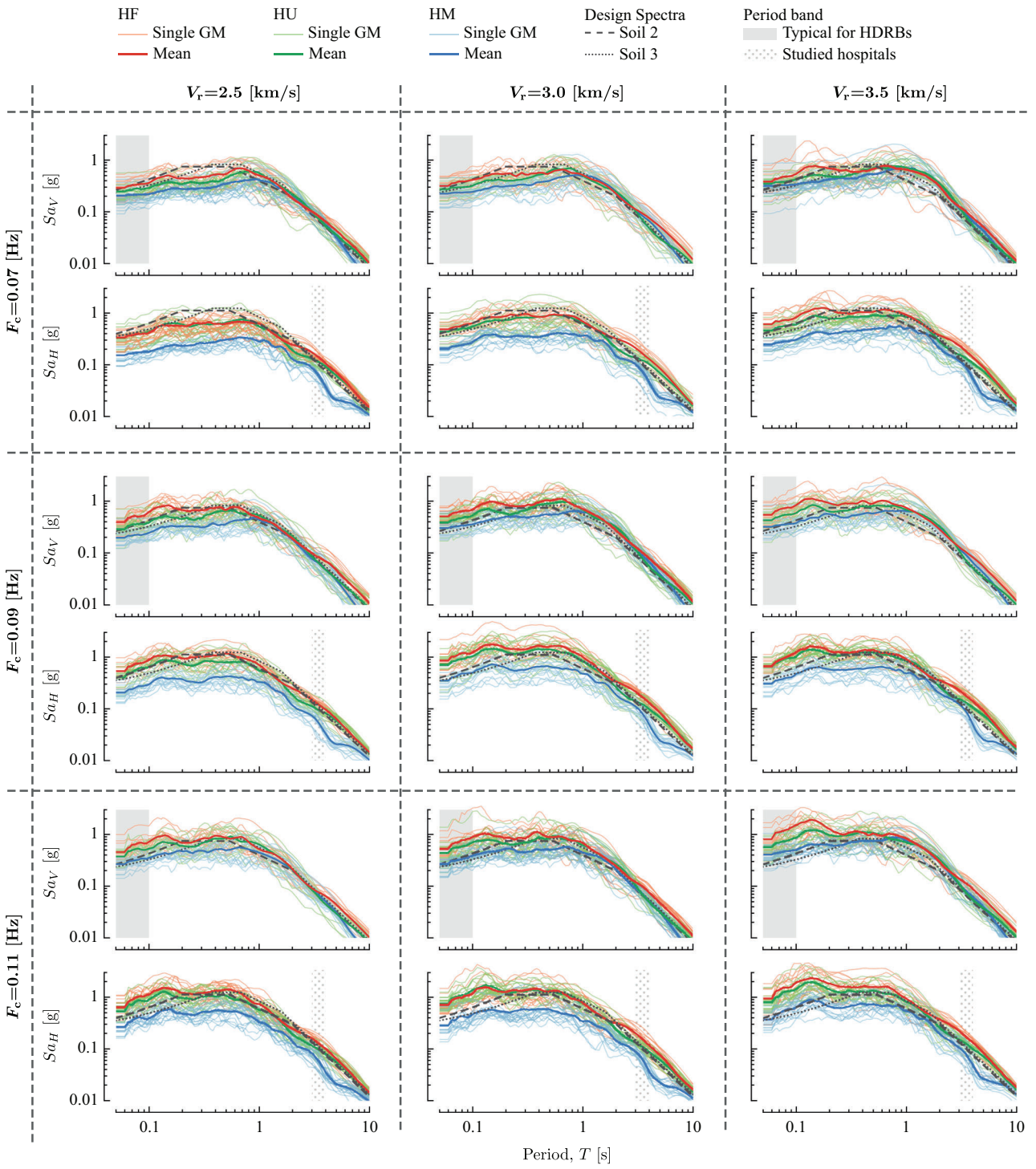


FIGURE 6 | Vertical ($Sa_V(T)$) and horizontal RotD100 pseudo-acceleration response spectra ($Sa_H(T)$) with a critical damping ratio of 5% for the nine M_w 6.9 earthquake scenarios, evaluated at the locations of the three BI hospitals. For each scenario, thin colored lines depict spectra from individual GM realizations, while thick colored lines represent the mean spectrum of the 16 realizations. The Chilean seismic design spectra for soil types 2 and 3 (corresponding to the hospital sites) are included for comparison (dashed lines). Grey shaded areas depict typical vertical period ranges for HDRBs and the fundamental periods of the studied hospitals in the vertical and horizontal GM spectra, respectively.

distance (12.0 km), M_w 6.9 earthquakes also result in PGAs larger than the design spectrum for all source combinations. In the case of $Sd_H(T_1)$ and $Sa_H(T_1)$, the source parameter combinations with V_r of 2.5 km/s and F_c of 0.09 or 0.11 Hz yield demands lower than those used in the design, all other scenarios generate larger demands. For the HM, the farthest from the fault trace (24.0 km), M_w 6.9 scenarios generate PGA_H demands larger than the design spectrum only when the rupture velocity is 3.0 km/s and the corner frequency is 0.09 Hz, and when the rupture velocity is 3.5 km/s combined with corner frequencies of 0.09 and 0.11 Hz. The $Sd_H(T_1)$ and $Sa_H(T_1)$ are lower than the computed value from the design spectrum for all source parameter combinations.

10969845, 0, Downloaded from https://onlinelibrary.wiley.com/doi/10.1002/eqe.70154 by Tu Delft, Wiley Online Library on [17/03/2026]. See the Terms and Conditions (https://onlinelibrary.wiley.com/terms-and-conditions) on Wiley Online Library for rules of use; OA articles are governed by the applicable Creative Commons License

TABLE 6 | IMs computed from the mean horizontal RotD100 pseudo-acceleration response spectra for all nine M_w6.9 earthquake scenarios, evaluated at the locations of the three BI hospitals.

			HF ($T_1 = 3.389$ s)			HU ($T_1 = 3.139$ s)			HM ($T_1 = 3.415$ s)		
M_w	V_r	F_c	PGA_H [g]	$Sd_H(T_1)$ [m]	$Sa_H(T_1)$ [g]	PGA_H [g]	$Sd_H(T_1)$ [m]	$Sa_H(T_1)$ [g]	PGA_H [g]	$Sd_H(T_1)$ [m]	$Sa_H(T_1)$ [g]
6.9	2.5	0.07	0.337	0.416	0.141	0.333	0.308	0.125	0.153	0.184	0.063
		0.09	0.535	0.356	0.121	0.409	0.261	0.106	0.206	0.160	0.055
		0.11	0.642	0.376	0.127	0.537	0.270	0.110	0.267	0.175	0.060
	3.0	0.07	0.484	0.494	0.167	0.439	0.325	0.132	0.205	0.222	0.076
		0.09	0.851	0.499	0.169	0.712	0.333	0.135	0.351	0.246	0.084
		0.11	0.712	0.462	0.156	0.760	0.304	0.123	0.282	0.187	0.064
	3.5	0.07	0.610	0.548	0.185	0.463	0.371	0.150	0.244	0.270	0.092
		0.09	0.668	0.537	0.182	0.665	0.366	0.148	0.307	0.269	0.092
		0.11	0.948	0.510	0.172	0.795	0.350	0.142	0.368	0.235	0.080
Design spectrum			0.300	0.300	0.101	0.300	0.300	0.122	0.300	0.330	0.113

Note: The presented IMs are: PGA_H, spectral displacement at the fundamental period ($Sd_H(T_1)$), and spectral pseudo-acceleration at the fundamental period ($Sa_H(T_1)$). Values from the Chilean design spectrum are also provided for comparison purposes.

Additionally, the demands from the other magnitude scenarios scale with event size. The M_w6.5 scenarios yield lower demands than those shown in Figure 6 and Table 6, while the M_w7.2 scenarios yield significantly larger demands, as detailed in the Supporting Material.

4.2 | Structural Response

The structural response of the three BI hospitals is presented, evaluating the behavior of the seismic isolation systems and the superstructures. The analysis focuses on five key EDPs as follows: the peak lateral displacement of the isolation layer, $u_{SI_{max}}$ (Figure 7), also showing an example of the normalized shear force versus lateral displacement, $V_{SI}/W(u_{SI})$ Figure 8); tensile forces in the isolation devices (Figure 9); development of cavitation in HDRBs (Figure 10); peak interstory drift, δ_{max} (Figure 11); and peak floor accelerations, $\ddot{u}_{max}$ (Figure 12). All superstructure response parameters are measured at the center of mass of each slab. These EDPs are fundamental to understanding the building behavior and their capacity to meet expected performance objectives, especially given the unique characteristics of the SRF events.

Figure 7 presents the peak lateral displacements of the isolation system ($u_{SI_{max}}$) for the three BI hospitals and the nine M_w6.9 earthquake scenarios, disaggregated in *X*- and *Y*-directions (see Figures S3 and S4 for M_w6.5 and M_w7.2, respectively). The maximum total displacements (gap between the isolated structure and surrounding retaining walls or fixed obstructions), u_{mce} (see Table 1), are also included as performance thresholds. Notice that the numerical models did not include gap elements to simulate physical impact. Therefore, displacement demands exceeding u_{mce} indicate collision with the surrounding retaining wall, but the complex post-impact dynamic behavior is not simulated. For the HF, the closest to the fault, several realizations across all M_w6.9 scenarios generate displacements that exceed u_{mce}. Note that displacements in the *Y*-direction are larger than those in the *X*-direction. For V_r of 3.0 km/s and particularly 3.5 km/s, the median displacements extend beyond u_{mce}, showing an increase in median responses with larger rupture velocities. Conversely, the HU shows median displacements that remain below u_{mce} across all parameter combinations. However, individual GM from each scenario exceeds that value, providing a non-negligible probability of impact despite lower median responses. The HM, being the furthest, shows displacements lower than u_{mce}, a minimum number of realizations for V_r of 3.5 km/s and F_c of 0.07 Hz exceeds such value. Furthermore, the interquartile range of the boxplots decreases as the distance from the SRF trace increases, indicating that the record-to-record variability is more pronounced for hospitals closer to the trace. These results suggest that the seismic isolation systems of hospitals in proximity to the SRF, such as HF and HU, are prone to reaching or exceeding such critical displacement under M_w6.9 crustal earthquake scenarios, especially for those with higher rupture velocities and corner frequencies, potentially compromising their intended performance objectives related to preventing impact with surrounding retaining walls.

To further examine the behavior of the isolation systems under extreme demands, Figure 8 illustrates the normalized total shear force–displacement (V_{SI}/W (u_{SI})) hysteresis for a representative simulation. The response across the three facilities highlights distinct levels of demand relative to their design capacities. While the isolation system in HM remains well within the seismic gap, HU reaches the threshold, and HF clearly exceeds the maximum design displacement u_{mce}. Notice that the exceedance of the u_{mce} limit in HF and HU indicates physical impact with the surrounding retaining (moat) walls. A collision with the retaining wall would result in sudden acceleration spikes and a significant amplification of interstory drift demands and floor accelerations.

10969845, 0, Downloaded from https://onlinelibrary.wiley.com/doi/10.1002/eqe.70154 by Tu Delft, Wiley Online Library on [17/03/2026]. See the Terms and Conditions (https://onlinelibrary.wiley.com/terms-and-conditions) on Wiley Online Library for rules of use; OA articles are governed by the applicable Creative Commons License

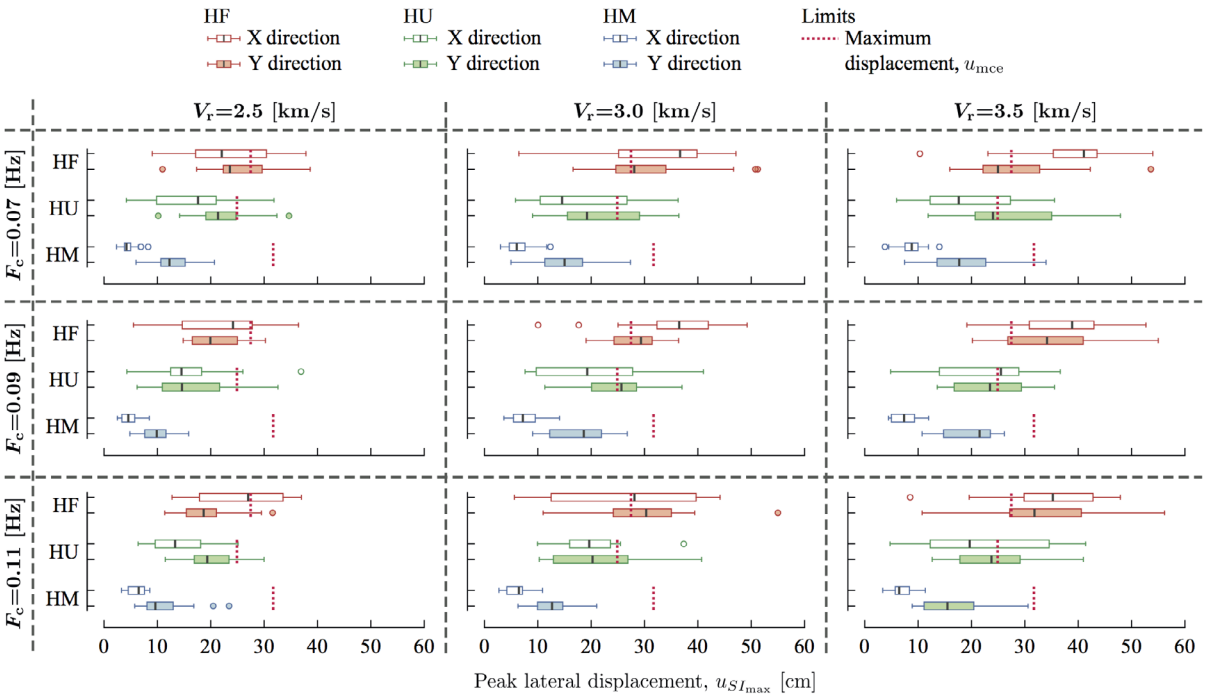


FIGURE 7 | Boxplot of peak lateral displacements of the isolation system ($u_{SI_{max}}$) in both directions for the three BI hospitals and the nine M_w6.9 earthquake scenarios.

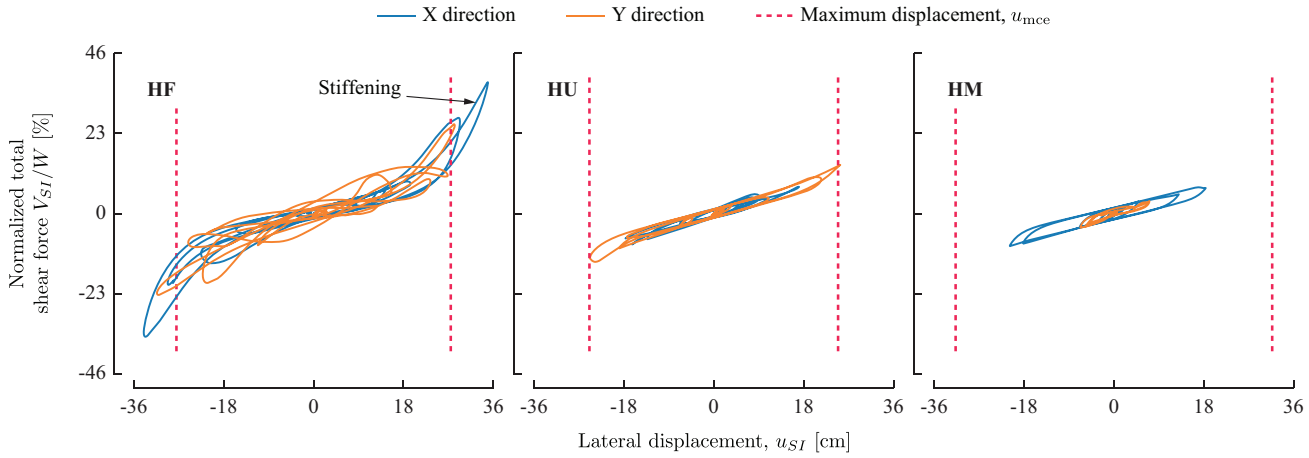


FIGURE 8 | Normalized shear force versus lateral displacement ($V_{SI}/W(u_{SI})$) of the isolation system for one simulation (M_w 6.9, V_r of 3.5 km/s, F_c of 0.09 Hz).

Notice that the hysteresis for HF exhibits significant stiffening as the lateral displacement surpasses the u_{mce} limit. This stiffening behavior, characteristic of HDRBs at large shear strains, is accurately captured by the calibrated nonlinear models. This stiffening effect results in a sharp increase in the base shear transmitted to the superstructure, which explains the amplified interstory drift demands and floor accelerations observed in the most critical near-fault scenarios (which is presented later).

Figure 9 shows the probability of isolation devices experiencing tensile forces for the nine M_w6.9 earthquake scenarios (all devices were included in the computation), a critical performance metric because such loads can cause damaging effects like cavitation in HDRBs or uplifting in SLs and, consequently, compromise the integrity of the device (see Figures S5 and S6 for M_w6.5 and M_w7.2, respectively). To quantify this risk, the state of each device was monitored throughout each simulation. The metric for each GM is the maximum percentage of devices that were simultaneously under tension at any single instant. The figure then shows the probability—calculated from the 16 realizations per scenario—of this peak percentage falling into predefined ranges: 0%, 0%–10%, 10%–20%, 20%–30%, and >30%. An increasing percentage of devices under tensile forces generally correlates with larger overall tensile demands on the isolation layer. The HF is very susceptible to tensile forces in the isolation system due to its proximity to the fault trace, resulting from the large vertical accelerations (see Figure 6). Even for the lowest intensity (V_r= 2.5 km/s, F_c= 0.07 Hz), there is only a 43.75% probability that

10969845, 0, Downloaded from https://onlinelibrary.wiley.com/doi/10.1002/eqe.70154 by Tu Delft, Wiley Online Library on [17/03/2026]. See the Terms and Conditions (https://onlinelibrary.wiley.com/terms-and-conditions) on Wiley Online Library for rules of use; OA articles are governed by the applicable Creative Commons License

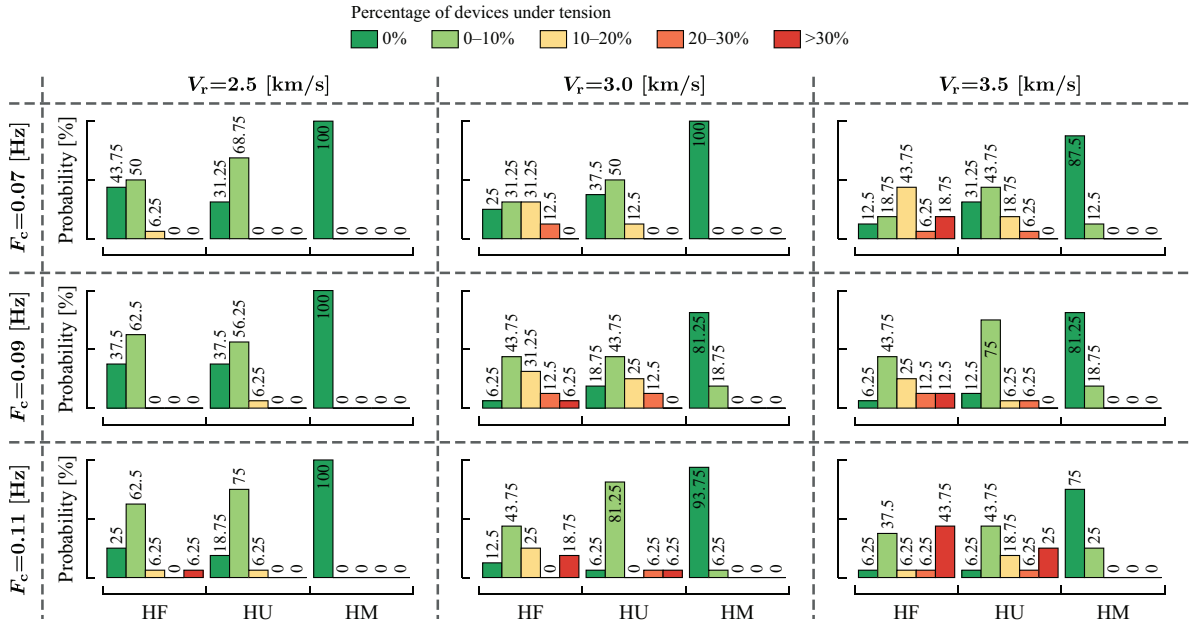


FIGURE 9 | Probability of tensile forces in the isolation devices for the three BI hospitals and the nine M_w6.9 earthquake scenarios.

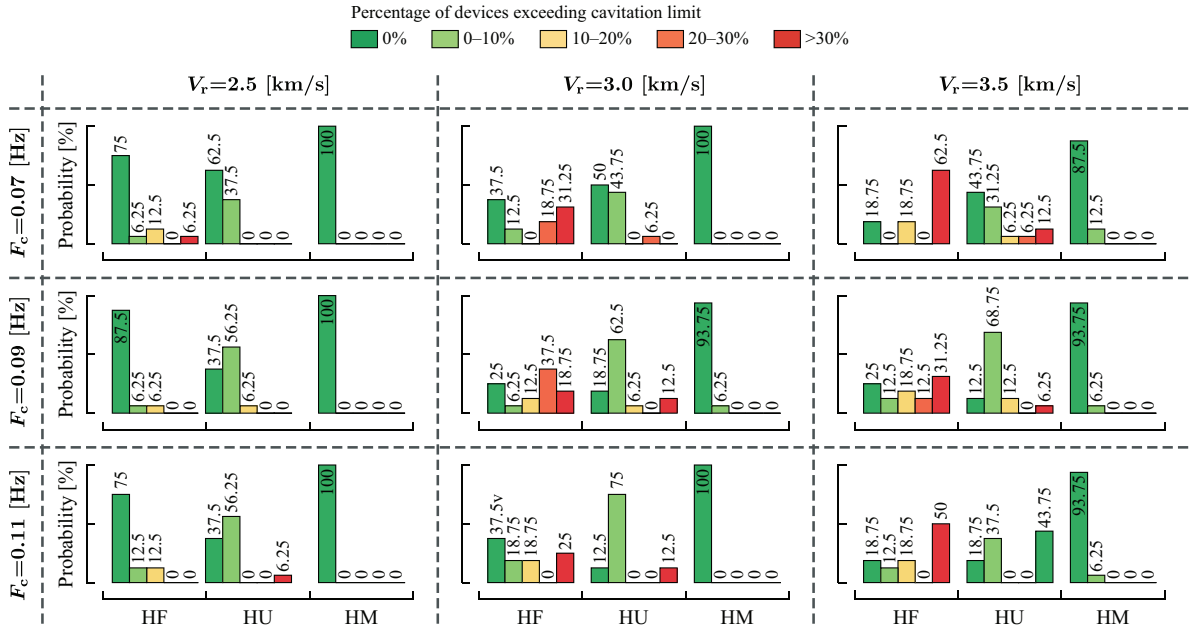


FIGURE 10 | Probability of HDRBs exceeding the cavitation threshold for the three BI hospitals and the nine M_w6.9 earthquake scenarios.

all devices remain under compression (i.e., 0% of devices under tensile forces). This probability decreases sharply with increasing V_r and F_c. Indeed, for the V_r= 3.5 km/s and F_c= 0.11 Hz scenario, the probability of zero devices under tension is 6.25%. For this scenario, the probability that more than 30% of the isolation devices experience tensile forces reaches a 43.75%. For the HU, the probabilities of tensile forces are comparatively lower than for the HF, as a consequence of its greater distance from the fault trace, but they remain significant across scenarios. While the probabilities of having all devices under compressive forces are often close to those of HF, the likelihood of a large percentage of devices (e.g., >30%) experiencing tension is reduced. For instance, in the V_r= 3.5 km/s and F_c= 0.11 Hz scenario, the probability of more than 30% of devices under tensile forces is 25%. The HM, being the furthest from the fault trace, demonstrates the lowest probability for tensile forces in the isolation device. For all scenarios, HM exhibits a high probability that 0% of devices are under tensile forces. Even in the most demanding scenario (V_r= 3.5 km/s, F_c= 0.11 Hz), there is a 75% chance of no tensile forces on the isolation system, and a 25% chance that less than 10% of the devices experience tensile forces.

Figure 10 presents the probability of HDRBs exceeding the cavitation threshold ($3G_rA_s$ [50], where A_s is the cross-section area of the device) for all three hospitals and nine M_w6.9 earthquake scenarios (see Figures S7 and S8 for M_w6.5 and M_w7.2, respectively).

10969845, 0, Downloaded from https://onlinelibrary.wiley.com/doi/10.1002/eqe.70154 by Tu Delft, Wiley Online Library on [17/03/2026]. See the Terms and Conditions (https://onlinelibrary.wiley.com/terms-and-conditions) on Wiley Online Library for rules of use; OA articles are governed by the applicable Creative Commons License

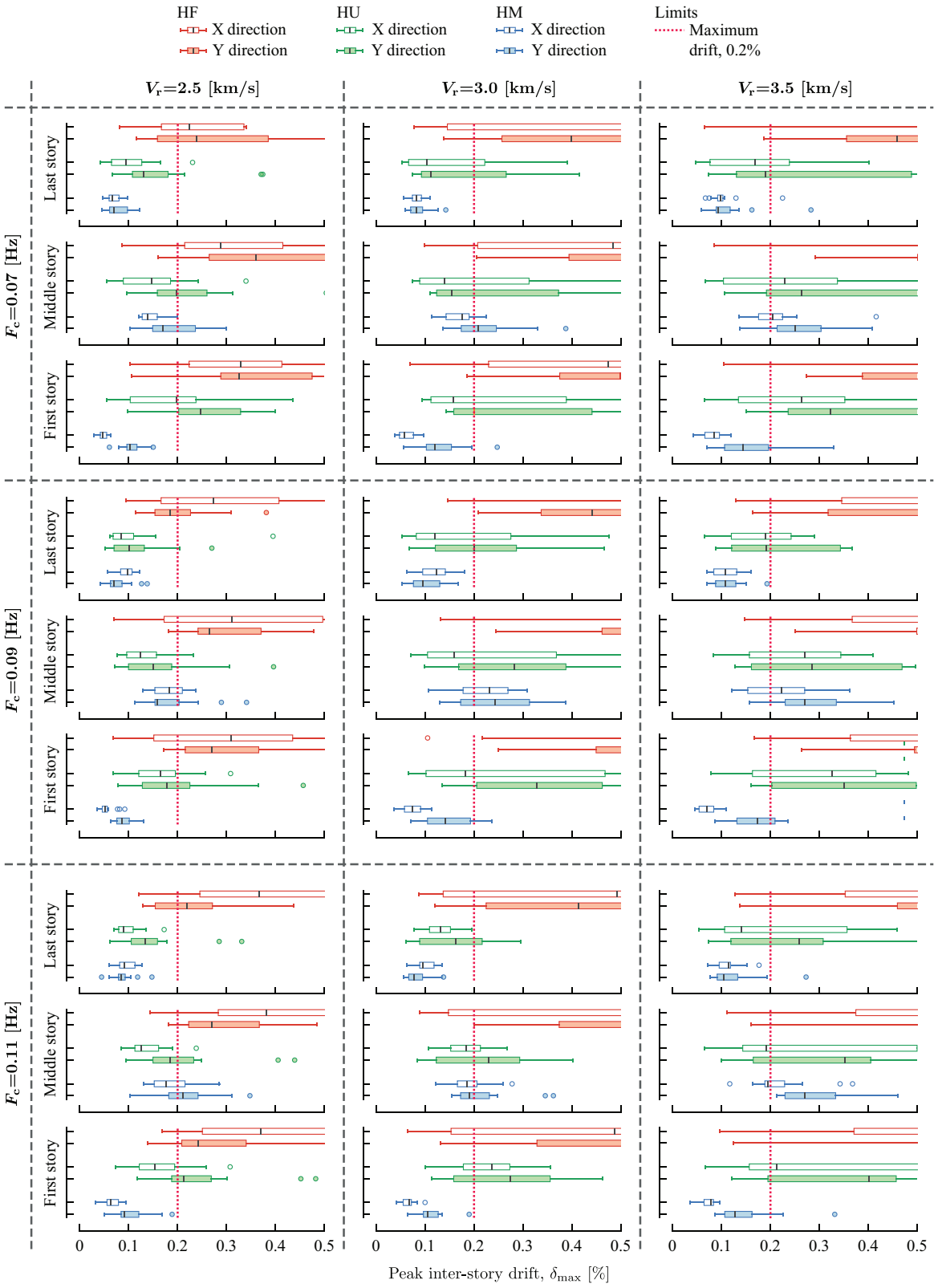


FIGURE 11 | Boxplot of peak interstory drift (δ_{max}) of the superstructure for the three BI hospitals and the nine M_w6.9 earthquake scenarios. The values for the first, middle, and last stories are plotted.

10969845, 0, Downloaded from https://onlinelibrary.wiley.com/doi/10.1002/eqe.70154 by Tu Delft, Wiley Online Library on [17/03/2026]. See the Terms and Conditions (https://onlinelibrary.wiley.com/terms-and-conditions) on Wiley Online Library for rules of use; OA articles are governed by the applicable Creative Commons License

This metric shows the percentage of HDRBs that experienced cavitation during the GM. The results show a clear sensitivity to both the rupture velocity (V_r) and the corner frequency (F_c). For hospital HF, an increase in rupture velocity from 2.5 to 3.5 km/s significantly shifts the response toward the higher cavitation categories; specifically, in the most critical scenarios ($V_r = 3.5$ km/s), there is a large probability that more than 30% of the HDRBs have experienced cavitation. In contrast, hospital HM maintains a nearly 100% probability of zero cavitation across nearly all simulated events. These findings suggest that for facilities like HF, the combined effect of large vertical accelerations and significant overturning moments—inherent to near-fault GMs—imposes a critical risk of internal bearing damage.

Figure 11 shows the peak interstory drifts (δ_{max}) for the three BI hospitals across the different M_w6.9 earthquake scenarios (see Figures S9 and S10 for M_w6.5 and M_w7.2, respectively). The results are presented for the first, mid-height, and upper stories, disaggregated in *X*- and *Y*-directions. The interstory drift is calculated as the ratio of the relative horizontal displacement between two consecutive slabs to the story height. The performance objective of these buildings is continuous operativity, establishing an interstory drift limit of 0.2%, which is included in the plots for comparison purposes. For the HF, the median interstory drifts exceed the 0.2% limit across all scenarios and story levels, reaching values beyond 0.5%. These large interstory drifts are a direct consequence of the large displacements at the isolation layer. At such displacement levels, the isolation devices exhibit significant stiffening (see Figure 8), transmitting much larger forces to the superstructure. The HU also demonstrates a tendency for interstory drifts to exceed the 0.2% limit, especially for lower and median stories. This is more evident for higher rupture velocities and corner frequencies, where the median drifts are significantly beyond the limit. The HM shows lower interstory drifts compared with the other two hospitals. The critical story is located at mid-height, where larger demands are observed. In general, median values are around 0.2% at this story, increasing with the V_r and F_c. However, all scenarios show individual realizations extending beyond the drift limit, these occurrences are of smaller magnitude compared to HF and HU, indicating a better performance of its superstructure. Across all hospitals, a general trend of increasing interstory drifts with increasing rupture velocity is noticed, particularly for higher corner frequencies. The exceedance of the 0.2% interstory drift limit for HF and HU highlights a potential challenge to their immediate occupancy performance objective under these specific crustal earthquake scenarios.

Table 7 presents the median interstory drift values, which confirm the trends observed in Figure 11. A first observation is the strong correlation between rupture velocity (V_r) and structural demand: as V_r increases from 2.5 to 3.5 km/s, the median drifts for HF shift from the operational range (< 0.5%) to values that indicate significant structural distress. For the $V_r = 3.5$ km/s and $F_c = 0.07$ Hz scenario, the *Y*-direction drift in the middle and last stories of HF reaches 1.323% and 1.629%, respectively—values that exceed the 0.75%–1.0% limit, which is a common threshold for the assumption of linear elastic validity in RC frames [60]. This suggests that the linear models likely underestimate the true displacements for these critical cases, as the superstructure would physically enter a nonlinear regime characterized by localized damage. Furthermore, the data highlight a notable directionality effect, with *Y*-direction demands frequently exceeding *X*-direction demands.

Figure 12 presents the peak floor absolute accelerations for the three BI hospitals across the M_w6.9 earthquake scenarios, for the isolation and roof slabs in *X*- and *Y*-directions (see Figures S11 and S12 for M_w6.5 and M_w7.2, respectively). An acceleration limit of 3.0 m/s^2 (0.31 g) is also included in the plots as a benchmark for performance assessment, demands exceeding this value can lead to a non-negligible probability of failure in critical components, such as anesthesia machines and ventilators [61], which are crucial for maintaining the continuous operativity performance objective of healthcare facilities following a seismic event. For all three hospitals, the peak floor accelerations increase with the story level (accelerations are larger for the roof slab compared with the isolation slab). For the HF, peak floor accelerations on both slabs are close to or exceed the 3.0 m/s^2 limit across most scenarios. The median accelerations for HF, particularly in the *Y*-direction, are beyond this threshold. The HU also demonstrates a tendency for peak floor accelerations to exceed the 3.0 m/s^2 limit. However, median peak accelerations of most seismic scenarios are lower than the limit. The exceedance is more common with increasing rupture velocities and corner frequencies. In contrast, the HM generally shows peak floor accelerations that remain well below the 3.0 m/s^2 limit across all scenarios and for both the isolation and roof slabs. The median accelerations for HM are consistently low, and just some individual realizations exceed 3.0 m/s^2. The widespread and frequent exceedance of the 3.0 m/s^2 peak floor acceleration limit for HF and HU highlights a potential damage to acceleration-sensitive equipment and nonstructural elements in these facilities.

5 | Discussion

The characterization of seismic hazard shows that for hospitals located closer to the SRF trace—specifically HF and HU—the simulated M_w6.9 earthquakes generate demands that exceed those prescribed by the current Chilean design code [23], particularly around the fundamental vibration periods of the isolated structures (see Figure 6). However, several source parameter combinations also lead to demands larger than those currently used in design for shorter periods. These differences suggest that current seismic design standards may be underestimating the seismic hazard in specific areas of the MRS. Additionally, the observed increase in spectral demands with higher rupture velocities and corner frequencies emphasizes the strong influence of these source parameters on local hazard intensity.

The structural response analyses highlight critical vulnerabilities in the new generation of Chilean healthcare facilities. The isolation systems demonstrate poor performance under GMs from crustal earthquakes, which is expected given they were designed for GM with other characteristics. Regarding peak lateral displacements of the isolation layer (see Figure 7), demands of HF and HU frequently exceed the total maximum displacement, u_{mce}, which represents the distance to retaining walls. This implies a high probability of physical impact with the surrounding retaining walls. The severity of such an impact is intrinsically linked to the exceedance magnitude: while a minor exceedance

10969845, 0, Downloaded from https://onlinelibrary.wiley.com/doi/10.1002/eqe.70154 by Tu Delft, Wiley Online Library on [17/03/2026]. See the Terms and Conditions (https://onlinelibrary.wiley.com/terms-and-conditions) on Wiley Online Library for rules of use; OA articles are governed by the applicable Creative Commons License

TABLE 7 | Median interstory drifts for M_w6.9 earthquake scenarios for all three BI hospitals.

	Hospital					
	HF		HU		HM	
Story	***X***	***Y***	***X***	***Y***	***X***	***Y***
$M_w6.9, V_r = 2.5, F_c = 0.07$						
First story	0.326	0.328	0.247	0.198	0.102	0.047
Middle story	0.360	0.289	0.197	0.146	0.170	0.139
Last story	0.239	0.223	0.131	0.094	0.070	0.066
$M_w6.9, V_r = 2.5, F_c = 0.09$						
First story	0.270	0.309	0.178	0.166	0.087	0.052
Middle story	0.266	0.311	0.150	0.124	0.158	0.183
Last story	0.185	0.273	0.101	0.084	0.069	0.098
$M_w6.9, V_r = 2.5, F_c = 0.11$						
First story	0.243	0.369	0.212	0.153	0.091	0.063
Middle story	0.271	0.382	0.185	0.125	0.211	0.177
Last story	0.219	0.367	0.134	0.089	0.085	0.091
$M_w6.9, V_r = 3.0, F_c = 0.07$						
First story	0.499	0.474	0.200	0.158	0.120	0.057
Middle story	0.551	0.483	0.154	0.140	0.209	0.176
Last story	0.399	0.527	0.111	0.103	0.083	0.083
$M_w6.9, V_r = 3.0, F_c = 0.09$						
First story	0.557	0.809	0.328	0.183	0.142	0.074
Middle story	0.639	0.901	0.282	0.159	0.243	0.232
Last story	0.441	0.896	0.201	0.120	0.095	0.123
$M_w6.9, V_r = 3.0, F_c = 0.11$						
First story	0.552	0.488	0.273	0.236	0.105	0.068
Middle story	0.618	0.536	0.230	0.184	0.191	0.186
Last story	0.413	0.492	0.163	0.131	0.077	0.096
$M_w6.9, V_r = 3.5, F_c = 0.07$						
First story	0.554	0.971	0.323	0.264	0.145	0.085
Middle story	0.636	1.323	0.263	0.229	0.251	0.205
Last story	0.459	1.629	0.190	0.168	0.093	0.097
$M_w6.9, V_r = 3.5, F_c = 0.09$						
First story	0.763	0.743	0.351	0.326	0.173	0.071
Middle story	0.857	0.882	0.286	0.270	0.271	0.223
Last story	0.723	0.873	0.191	0.190	0.108	0.108
$M_w6.9, V_r = 3.5, F_c = 0.11$						
First story	0.723	0.647	0.401	0.214	0.127	0.078
Middle story	0.864	0.725	0.352	0.192	0.270	0.196
Last story	0.788	0.912	0.260	0.142	0.105	0.114

results in low-velocity contact with localized effects, the large exceedances observed in HF imply high-velocity impacts. Such collision increases the risk of physical damage to the isolation devices (e.g., sliders impacting their outer rings). More critically, from a functional perspective, this implies that the system can no longer provide the intended seismic performance [20]. Furthermore, the impact effect is propagated to the superstructures, generating large acceleration spikes [19] and interstory drifts [18], damaging acceleration-sensitive medical equipment and nonstructural components, as well as structural elements. This would effectively compromise the hospital's ability to maintain continuous operations immediately after the event. Furthermore,

10969845, 0, Downloaded from https://onlinelibrary.wiley.com/doi/10.1002/eqe.70154 by Tu Delft, Wiley Online Library on [17/03/2026]. See the Terms and Conditions (https://onlinelibrary.wiley.com/terms-and-conditions) on Wiley Online Library for rules of use; OA articles are governed by the applicable Creative Commons License

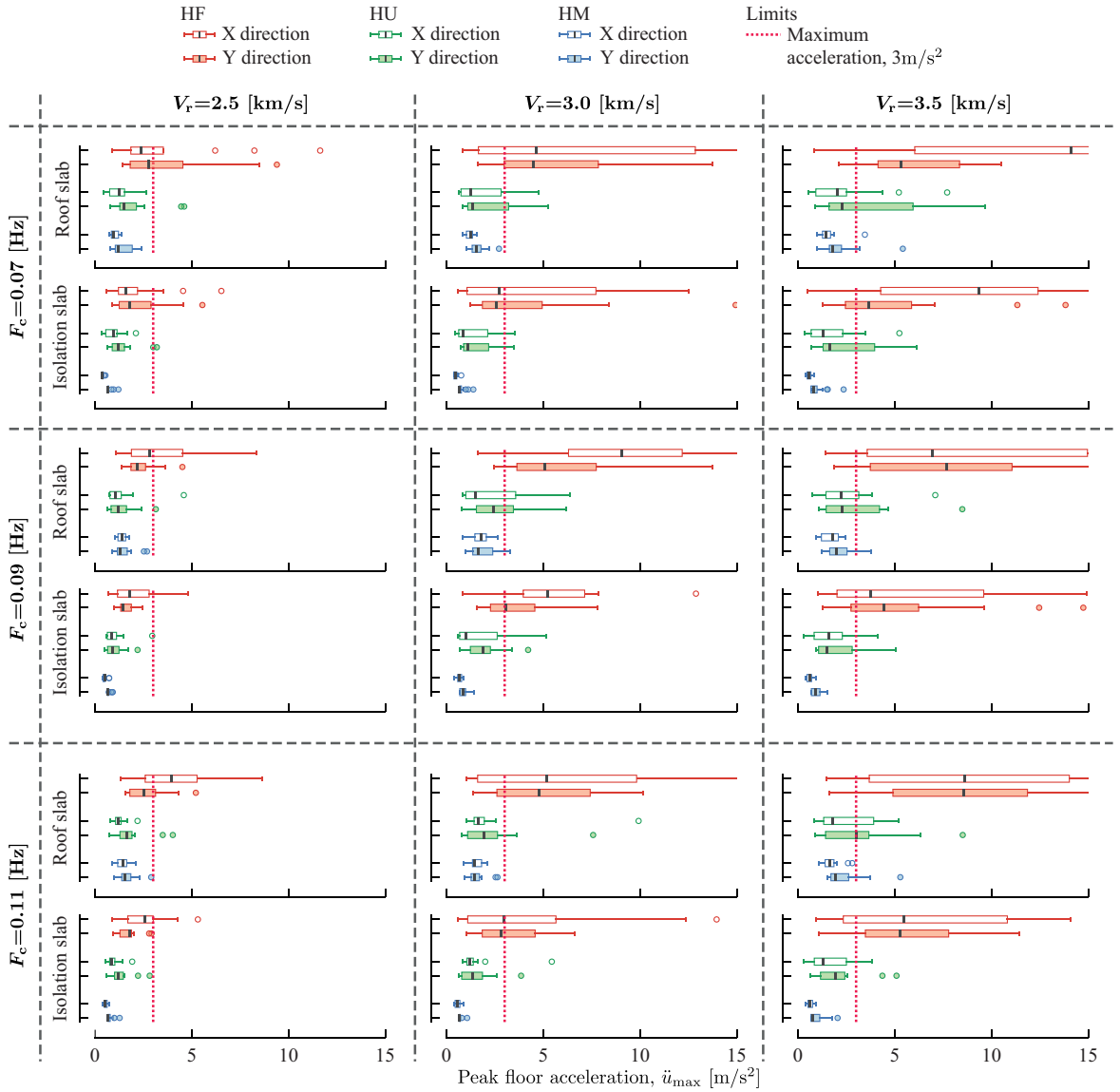


FIGURE 12 | Boxplot of peak floor accelerations ($\ddot{u}_{max}$) of the superstructure for the three BI hospitals and the nine M_w6.9 earthquake scenarios. The values for the isolation slab and roof slab are plotted.

the analysis of tensile forces in the isolation devices (see Figure 9) reveals a significant likelihood of tensile forces for HF and HU. This behavior is attributed to the large vertical accelerations and overturning of the building. Such tensile forces lead to cavitation the HDRBs (see Figure 10), potentially compromising their structural integrity. Attempts to use explicit nonlinear friction elements for the sliders (SLs) in HU resulted in numerical instability due to the loss of contact and subsequent impact in the SLs. The decision of using an effective linear stiffness allowed for the completion of the sensitivity analysis, but the convergence difficulties themselves underscore a critical finding: the vertical hazard of the SRF may exceed the operational limits of traditional sliding interfaces. Beyond the isolation layer, interstory drifts (see Figure 11) for these facilities exceed the design limit of 0.2% for most earthquake scenarios, which is a critical threshold for minimizing nonstructural damage and ensuring post-earthquake functionality. These exceedances are mainly in the lower and mid-height stories, areas that are typically dedicated to emergency departments. Furthermore, peak floor accelerations (see Figure 12) in HF and HU frequently exceed 3.0 m/s^2, which is a representative limit for protecting acceleration-sensitive nonstructural components and equipment. The combination of excessive interstory drifts and large floor accelerations suggests a high probability of significant damage to medical equipment and architectural components, which could render critical areas of these hospitals inoperable despite the use of base isolation. Collectively, the results indicate that the performance observed among the three hospitals directly correlates with their proximity to the SRF, as expected. HM, being the farthest, shows more favorable seismic performance across all metrics, highlighting the strong spatial dependence. Thus, facilities within approximately 15 km of the fault trace are at significantly higher risk due to earthquakes generated by the SRF. Although BI is a robust technique that enhances building performance, these results demonstrate its limitations when this system was not designed for GM of these characteristics, especially concerning the vertical component that can induce tensile forces. Finally, it is well-known that the intensity of the hazard and its consequences

10969845, 0, Downloaded from https://onlinelibrary.wiley.com/doi/10.1002/eqe.70154 by Tu Delft, Wiley Online Library on [17/03/2026]. See the Terms and Conditions (https://onlinelibrary.wiley.com/terms-and-conditions) on Wiley Online Library for rules of use; OA articles are governed by the applicable Creative Commons License

are directly correlated with event magnitude, which was also observed in this research. The seismic response analyses for the M_w6.5 earthquake scenarios showed less demanding conditions, leading to a satisfactory performance of all three hospitals, where demand parameters remained within design limits. Conversely, the M_w7.2 scenarios generated extremely large demands, exceeding all established design limits for every hospital, highlighting a critical vulnerability at higher magnitudes. Therefore, determining the maximum possible earthquake to be generated by the SRF is a critical aspect to be studied.

Additionally, it is important to acknowledge certain limitations of this study. The superstructure was assumed to remain linear-elastic. While this behavior is expected in most scenarios, the elastic limit may be exceeded (0.75%–1.0% [60]) under the most extreme events. Furthermore, the numerical models did not explicitly simulate the physical impact between the isolation system and the retaining wall. While displacement limits were used to identify potential collisions, the study does not capture the shock waves and increased interstory drifts that would result from such impacts. The physics-based GM simulations, while advanced, are still subject to epistemic uncertainties in fault parameters, some of them were addressed through a parametric sensitivity analysis. Furthermore, detailed soil–structure interaction effects beyond simplified soil types were not explicitly modeled. Despite these limitations, this research provides valuable data suggesting that the seismic hazard of the SRF requires a re-evaluation of current design practices and risk assessment strategies for all structures and infrastructure in the MRS. Currently, the design spectra are derived primarily from historical subduction megathrust events, neglecting potential GMs from crustal faults. The findings of this study indicate that these provisions may be insufficient for structures located near active crustal faults, as they do not explicitly account for near-fault effects such as long-period velocity pulses and large vertical accelerations. Similarly, there is a significant need for updated design and risk assessment strategies for structures in the proximity of active crustal faults worldwide. This is because current probabilistic seismic risk frameworks may suggest that hospital performance is acceptable due to the extremely low seismicity rates of certain faults—such as the SRF—potentially overlooking the consequences of a rare, crustal earthquake.

6 | Conclusions

This study evaluates the seismic performance of three of the new generation of seismically isolated hospitals in the Metropolitan Region of Santiago (MRS), Chile, under potential earthquakes generated along the San Ramón fault (SRF). Given the limited information about the seismigenic capacity of the seismic source, physics-based earthquake simulations were employed along with an uncertainty approach for the source parameters—including event magnitude, average rupture velocity, and corner frequency—resulting in 27 earthquake scenarios and 16 realizations each (432 in total). The performance assessment, using nonlinear 3D FE models, provides critical insights into the vulnerability of the healthcare facilities to this recently declared active hazard. Based on the results, the following conclusions are drawn:

- The M_w6.9 earthquake scenarios generate GM demands exceeding those prescribed by the current Chilean design standard for structures close to the SRF (distances lower to 15.0 km). This suggests a potential underestimation of the seismic hazard by existing design provisions for structures exposed to this, and other crustal faults. Furthermore, increased rupture velocities and corner frequencies invariably led to higher spectral demands and, consequently, greater seismic response in the structures
- For M_w6.9 earthquake scenarios, despite their efficiency, the isolation systems fail to meet their performance objectives when subjected to earthquakes from the SRF, particularly for structures near the fault trace (< 15 km). Peak lateral displacements of the isolation layer exceed their design limits, providing a high probability of impact with retaining walls. Furthermore, large vertical accelerations and overturning moments induce significant tensile forces, leading to a high likelihood of cavitation in HDRBs and potentially compromising the stability and load-carrying capacity of the isolation layer.
- For M_w6.9 earthquake scenarios, the superstructure response of hospitals near the fault (< 15 km) hinders the objective of continuous operativity. Interstory drifts frequently exceeded the 0.2% limit that is established by the design code, and for some scenarios, exceed the range where linear-elastic assumption is valid (0.75%–1.0%). Similarly, peak floor accelerations are larger than 3.0 m/s^2, triggering damage in acceleration-sensitive nonstructural components and equipment. The combination of these excessive drifts and accelerations suggests a high probability of damage to medical equipment and architectural components, jeopardizing the functionality of critical hospital areas like emergency departments.
- Seismic demands are strongly dependent on the event magnitude and source parameters. The results, partially presented in the supporting material, show that: M_w6.5 scenarios generate small demands, while M_w7.2 scenarios provide extremely large demands, potentially leading to extensive damage. Consequently, reducing epistemic uncertainty regarding the maximum magnitude and rupture characteristics of the SRF is critical for future risk assessment.

Future work should focus on refining the knowledge about the seismogenic capacity of the SRF and including conventional fixed-base buildings to provide a broader comparison of regional vulnerability, as well as including nonlinear behavior in the superstructure. This will allow the development of mitigation strategies, potentially defining safer zones or even exclusion zones for construction, and enhancing the seismic resilience of the MRS.

Author Contributions

José A. Gallardo: conceptualization, methodology, software, validation, investigation, visualization, writing – original draft, writing – reviewand editing. **Matías F. Chacón:** conceptualization, software, investigation, visualization, writing – original draft, writing – review and editing. **Juan P. Muñoz:** methodology, visualization, writing – review and editing.

10969845, 0, Downloaded from https://onlinelibrary.wiley.com/doi/10.1002/eqe.70154 by Tu Delft, Wiley Online Library on [17/03/2026]. See the Terms and Conditions (https://onlinelibrary.wiley.com/terms-and-conditions) on Wiley Online Library for rules of use; OA articles are governed by the applicable Creative Commons License

Fernando Gutiérrez-Urzúa: methodology, software, writing – review and editing. **José Cembrano:** conceptualization, writing – original draft, writing – review and editing, funding acquisition. **Tiziana Rossetto:** conceptualization, writing – review and editing, funding acquisition. **Fabio Freddi:** conceptualization, writing – review and editing, funding acquisition. **Jorge G. F. Crempien:** conceptualization, methodology, software, writing – original draft, writing – review and editing, funding acquisition. **Juan C. de la Llera:** conceptualization, methodology, investigation, supervision, writing – review and editing, funding acquisition.

Acknowledgments

This research has been sponsored by the 2022 Seed Fund UCL-PUC research initiative and ANID, under the ANID/ doctorate scholarship/ 21201370; Research Center for Integrated Disaster Risk Management (CIGIDEN), ANID/ FONDAP/ 1523A0009; FONDECYT project, Multi-scale earthquake risk mitigation of healthcare networks using seismic isolation, ANID/ FONDECYT/ 1220292; and anillo project EASER (Evolution Assessment of Seismic Risk), ANID/ACT240044. The authors are grateful for all this support.

Conflicts of Interest

The authors declare no conflicts of interest.

Data Availability Statement

The datasets generated and analyzed during the current study are available from the corresponding author on reasonable request.

References

1. P. Jarrin, J.-M. Nocquet, F. Rolandone, H. Mora-Páez, P. Mothes, and D. Cisneros, "Current Motion and Deformation of the Nazca Plate: New Constraints From GPS Measurements," *Geophysical Journal International* 232, no. 2 (2022): 842–863, https://doi.org/10.1093/gji/ggac353.

2. S. Ruiz, S. Ide, B. Potin, and R. Madariaga, "Fast and Slow Subduction Earthquakes in Latin America," *Annual Review of Earth and Planetary Sciences* 53 (2025): 511–538, https://doi.org/10.1146/annurev-earth-040522-121945.

3. S. Ruiz and R. Madariaga, "Historical and Recent Large Megathrust Earthquakes in Chile," *Tectonophysics* 733 (2018): 37–56, https://doi.org/10.1016/j.tecto.2018.01.015.

4. J. de la Llera, J. Mitrani-Reiser, F. Rivera Jofre, et al., "The 2010 Chile Earthquake: A Five-Year Reflection," in *Proceedings of the 10th Pacific Conference on Earthquake Engineering* (AEES, 2015).

5. B. Simpson, P. Kakoty, M. Ortega, and W. Hassan, *Resilience Reconnaissance for Hospitals After the Maule Earthquake*, Technical Report (Earthquake Engineering Research Institute (EERI), 2018).

6. R. Armijo, R. Rauld, R. Thiele, G. Vargas, J. Campos, R. Lacassin, and E. Kausel, "The West Andean Thrust, the San Ramón Fault, and the Seismic Hazard for Santiago, Chile," *Tectonics* 29, no. 2 (2010), https://doi.org/10.1029/2008TC002427.

7. D. Díaz, A. Maksymowicz, G. Vargas, E. Vera, E. Contreras-Reyes, and S. Rebolledo, "Exploring the Shallow Structure of the San Ramón Thrust Fault in Santiago, Chile (∼ 33.5° S), Using Active Seismic and Electric Methods," *Solid Earth* 5, no. 2 (2014): 837–849, https://doi.org/10.5194/se-5-837-2014.

8. R. Rauld, "Deformación Cortical y Peligro Sísmico Asociado a la Falla San Ramón en el Frente Cordillerano de Santiago, Chile Central (33° S)" (Ph.D. diss., Universidad de Chile, 2011).

9. N. Pérez-Estay, G. Yáñez, S. Carretier, E. Lira, and J. Maringue, "Seismic Hazard in Low Slip Rate Crustal Faults, Estimating the Characteristic Event and the Most Hazardous Zone: Study Case San Ramón Fault, in Southern Andes," *Natural Hazards and Earth System Sciences* 16, no. 12 (2016): 2511–2528, https://doi.org/10.5194/nhess-16-2511-2016.

10. S. Yavari, S. Chang, and K. Elwood, "Modeling Post-Earthquake Functionality of Regional Health Care Facilities," *Earthquake Spectra* 26, no. 3 (2010): 869–892, https://doi.org/10.5194/nhess-16-2511-2016.

11. M. Bhandari, S. Bharti, M. Shrimali, and T. Datta, "Seismic Fragility Analysis of Base-Isolated Building Frames Excited by Near- and Far-Field Earthquakes," *Journal of Performance of Constructed Facilities* 33, no. 3 (2019): 04019029, https://doi.org/10.1061/(ASCE)CF.1943-5509.0001298.

12. A. Chanda and R. Debbarma, "Probabilistic Seismic Analysis of Base Isolated Buildings Considering Near and Far Field Earthquake Ground Motions," *Structure and Infrastructure Engineering* 18, no. 1 (2022): 97–108, https://doi.org/10.1080/15732479.2020.1836000.

13. F. Freddi, J. de la Llera, F. Gutiérrez-Urzúa, et al., "Seismic Response of Isolated Structures Under Subduction and Crustal Ground Motions: Analysis of a Case Study Structure," in *Proceedings of Conference Earthquake Risk and Engineering Towards a Resilient World* (Society for Earthquake and Civil Engineering Dynamics (SECED), 2023).

14. R. Jangid and J. Kelly, "Base Isolation for Near-Fault Motions," *Earthquake Engineering & Structural Dynamics* 30, no. 5 (2001): 691–707, https://doi.org/10.1002/eqe.31.

15. S. Bhagat, A. Wijeyewickrema, and N. Subedi, "Influence of Near-Fault Ground Motions With Fling-Step and Forward-Directivity Characteristics on Seismic Response of Base-Isolated Buildings," *Journal of Earthquake Engineering* 25, no. 3 (2021): 455–474, https://doi.org/10.1080/13632469.2018.1520759.

16. J. Gallardo and J. de la Llera, "Epistemic Uncertainty in the Seismic Performance Assessment of Isolated Buildings due to High Damping Rubber Bearing Model Selection," *Engineering Structures* 348 (2026): 121734, https://doi.org/10.1016/j.engstruct.2025.121734.

17. S. Kitayama and M. Constantinou, "Performance Evaluation of Seismically Isolated Buildings Near Active Faults," *Earthquake Engineering & Structural Dynamics* 51, no. 5 (2022): 1017–1037, https://doi.org/10.1002/eqe.3602.

18. D. Pant and A. Wijeyewickrema, "Structural Performance of a Base-Isolated Reinforced Concrete Building Subjected to Seismic Pounding," *Earthquake Engineering & Structural Dynamics* 41, no. 12 (2012): 1709–1716.

19. D. Pant and A. Wijeyewickrema, "Influence of Near-Fault Ground Motions on the Response of Base-Isolated Reinforced Concrete Buildings considering Seismic Pounding," *Advances in Structural Engineering* 16, no. 12 (2013): 1973–1988, https://doi.org/10.1260/1369-4332.16.12.1973.

20. A. Masroor and G. Mosqueda, "Experimental Simulation of Base-Isolated Buildings Pounding Against Moat Wall and Effects on Superstructure Response," *Earthquake Engineering & Structural Dynamics* 41, no. 14 (2012): 2093–2109, https://doi.org/10.1002/eqe.2177.

21. F. Mazza and A. Vulcano, "Effects of Near-Fault Ground Motions on the Nonlinear Dynamic Response of Base-Isolated R.C. Framed Buildings," *Earthquake Engineering & Structural Dynamics* 41, no. 2 (2012): 211–232, https://doi.org/10.1002/eqe.1126.

22. G. Giuliani, S. Sgobba, F. Micozzi, F. Ramadan, L. Ragni, G. Lanzano, L. Luzi, and A. Dall'Asta, "Combined Vertical and Horizontal Components of Near-Source Earthquakes and Impact on Base-Isolated Structures," *Earthquake Engineering & Structural Dynamics* 55, no. n/a (2026): 781–803, https://doi.org/10.1002/eqe.70109.

23. INN, *Analysis and Design of Buildings With Seismic Isolation*, Technical Report NCh433 (Instituto Nacional de Normalización, NCh433, 2013).

24. Instituto Nacional de Estadísticas de Chile, "Resultados censo 2024" (2025), censo2024.ine.gob.cl.

10969845, 0, Downloaded from https://onlinelibrary.wiley.com/doi/10.1002/eqe.70154 by Tu Delft, Wiley Online Library on [17/03/2026]. See the Terms and Conditions (https://onlinelibrary.wiley.com/terms-and-conditions) on Wiley Online Library for rules of use; OA articles are governed by the applicable Creative Commons License

25. G. Yáñez, N. Perez-Estay, J. Araya-Vargas, et al., "Shallow Anatomy of the San Ramón Fault (Chile) Constrained by Geophysical Methods: Implications for its Role in the Andean Deformation," *Tectonics* 39, no. 8 (2020): e2020TC006294, https://doi.org/10.1029/2020TC006294.

26. J. Brüggen, *Fundamentos de la geología de chile*, Technical Report (Instituto Geográfico Millitar, 1950).

27. J. Tricart, A. Hirsch, and J. Griesbach, "Géomorphologie et eaux souterraines dans le bassin de Santiago du Chili," *Bulletin de la Faculté des Lettres de l'Univ de Strasbourg* no. 413 (1967): 115–116, https://www.persee.fr/doc/geo_0003-4010_1967_num_76_413_14940.

28. A. Lavenu, R. Thiele, M. Machette, R. Dart, L.-A. Bradley, and K. Haller, *Maps and Database of Quaternary Faults in Bolivia and Chile*, Technical Report (U.S. Geological Survey, 2000), https://pubs.usgs.gov/of/2000/ofr-00-0283/ofr-00-0283.pdf.

29. D. Sellés and P. Gana, *Geología del área Talagante-San Francisco de Mostazal: Regiones Metropolitana de Santiago y del Libertador General Bernardo O'Higgins*, Technical Report (Servicio Nacional de Geología y Minería, 2001).

30. R. Rauld, "Análisis morfoestructural del frente cordillerano de Santiago Oriente, entre el Río Mapocho y la Quebrada de Macul" (2002).

31. G. Vargas, Y. Klinger, T. Rockwell, et al., "Probing Large Intraplate Earthquakes at the West Flank of the Andes," *Geology* 42, no. 12 (2014): 1083–1086, https://doi.org/10.1130/G35741.1.

32. J. Ammirati, G. Vargas, S. Rebolledo, et al., "The Crustal Seismicity of the Western Andean Thrust (Central Chile, 33°–34° S): Implications for Regional Tectonics and Seismic Hazard in the Santiago Area," *Bulletin of the Seismological Society of America* 109, no. 5 (2019): 1985–1999, https://doi.org/10.1785/0120190082.

33. INN, *Earthquake Resistant Design of Buildings*, Technical Report NCh433 (Instituto Nacional de Normalización, 2012).

34. Hospital Clínico Dra. Eloísa Díaz La Florida, *Cuenta pública participativa gestión 2023*, Technical Report (Hospital Clínico Dra. Eloísa Díaz, 2024).

35. Hospital de Urgencias Asistencia Pública, *Cuenta pública 2023*, Technical Report (Hospital de Urgencias Asistencia Pública, 2024).

36. Hospital El Carmen Dr. Luis Valentín Ferrada, *Cuenta pública participativa gestión 2023*, Technical Report (Hospital El Carmen Dr. Luis Valentín Ferrada, 2024).

37. F. McKenna, "OpenSees: A Framework for Earthquake Engineering Simulation," *Computing in Science and Engineering* 13, no. 4 (2011): 58–66, https://doi.org/10.1109/MCSE.2011.66.

38. J. Crempien and R. Archuleta, "UCSB Method for Simulation of Broadband Ground Motion From Kinematic Earthquake Sources," *Seismological Research Letters* 86, no. 1 (2015): 61–67, https://doi.org/10.1785/0220140103.

39. J. Crempien and R. Archuleta, "Within-Event and Between-Events Ground Motion Variability From Earthquake Rupture Scenarios," *Pure and Applied Geophysics* no. 174 (2017): 3451–3465, https://doi.org/10.1007/s00024-017-1615-x.

40. K. Aki and P. Richards, *Quantitative Seismology* (University Science Books, 2002).

41. N. Haskell, "Total Energy and Energy Spectral Density of Elastic Wave Radiation From Propagating Faults," *Bulletin of the Seismological Society of America* 54, no. 6A (1964): 1811–1841, https://doi.org/10.1785/BSSA05406A1811.

42. J. Schmedes, R. Archuleta, and D. Lavallée, "A Kinematic Rupture Model Generator Incorporating Spatial Interdependency of Earthquake Source Parameters," *Geophysical Journal International* 192, no. 3 (2012): 1116–1131, https://doi.org/10.1093/gji/ggs021.

43. M. Cario and B. Nelson, *Modeling and Generating Random Vectors With Arbitrary Marginal Distributions and Correlation Matrix*, Technical Report (Northwestern University, 1997), https://www.ressources-actuarielles.net/EXT/ISFA/1226.nsf/0/5d499a3efc8ae4dfc125756c00391ca6/$FILE/NORTA.pdf.

44. L. Zhu and L. Rivera, "A Note on the Dynamic and Static Displacements From a Point Source in Multilayered Media," *Geophysical Journal International* 148, no. 3 (2002): 619–627, https://doi.org/10.1046/j.1365-246X.2002.01610.x.

45. K. Aki, "Scaling Law of Seismic Spectrum," *Journal of Geophysical Research* 72, no. 4 (1967): 1217–1231, https://doi.org/10.1029/JZ072i004p01217.

46. M. Leonard, "Earthquake Fault Scaling: Self-Consistent Relating of Rupture Length, Width, Average Displacement, and Moment Release," *Bulletin of the Seismological Society of America* 100, no. 5A (2010): 1971–1988, https://doi.org/10.1785/0120090189.

47. S. Popovics, "Verification of Relationships Between Mechanical Properties of Concrete-Like Materials," *Matériaux et Construction* 8 (1975): 183–191, https://doi.org/10.1007/BF02475168.

48. A. Comittee, *Building Code Requirements for Structural Concrete and Commentary*, Technical Report 318R-19 (American Concrete Institute, 2019).

49. D. Grant, G. Fenves, and A. Whittaker, "Bidirectional Modelling of High-Damping Rubber Bearings," *Journal of Earthquake Engineering* 8, no. S1 (2004): 161–185, https://doi.org/10.1080/13632460409350524.

50. M. Kumar, A. Whittaker, and M. Constantinou, "An Advanced Numerical Model of Elastomeric Seismic Isolation Bearings," *Earthquake Engineering & Structural Dynamics* 43, no. 13 (2014): 1955–1974, https://doi.org/10.1002/eqe.2431.

51. C. Koh and J. Kelly, "A Simple Mechanical Model for Elastomeric Bearings Used in Base Isolation," *International Journal of Mechanical Sciences* 30, no. 12 (1988): 933–943, https://doi.org/10.1016/0020-7403(88)90075-6.

52. J. Kelly and D. Konstantinidis, *Mechanics of Rubber Bearings for Seismic and Vibration Isolation* (John Wiley & Sons, 2011).

53. American Society of Civil Engineers, *Minimum Design Loads and Associated Criteria for Buildings and Other Structures*, Tech. Rep. ASCE/SEI 7-22 (American Society of Civil Engineers, 2021).

54. S. Miranda, J. de la Llera, and E. Miranda, "Uncertainty on Measurement of Elastomeric Isolators Effective Properties," *Measurement* 180 (2021): 109511, https://doi.org/10.1016/j.measurement.2021.109511.

55. N. Hansen and A. Ostermeier, "Completely Derandomized Self-Adaptation in Evolution Strategies," *Evolutionary Computation* 9, no. 2 (2001): 159–195, https://doi.org/10.1162/106365601750190398.

56. N. Hansen, "The CMA Evolution Strategy: A Tutorial," preprint arXiv:1604.00772, 2016, https://doi.org/10.48550/arXiv.1604.00772.

57. K. Ryan and J. Polanco, "Problems With Rayleigh Damping in Base-Isolated Buildings," *Journal of Structural Engineering* 134, no. 11 (2008): 1780–1784, https://doi.org/10.1061/(ASCE)0733-9445(2008)134:11(1780).

58. H. Anajafi, R. Medina, and E. Santini-Bell, "Effects of the Improper Modeling of Viscous Damping on the First-Mode and Higher-Mode Dominated Responses of Base-Isolated Buildings," *Earthquake Engineering & Structural Dynamics* 49, no. 1 (2020): 51–73, https://doi.org/10.1002/eqe.3223.

59. D. Boore, "Orientation-Independent, Nongeometric-Mean Measures of Seismic Intensity From Two Horizontal Components of Motion," *Bulletin of the Seismological Society of America* 100, no. 4 (2010): 1830–1835, https://doi.org/10.1785/0120090400.

60. M. Priestley, "Brief Comments on Elastic Flexibility of Reinforced Concrete Frames and Significance to Seismic Design," *Bulletin of the New Zealand Society for Earthquake Engineering* 31, no. 4 (1998): 246–259, https://doi.org/10.5459/bnzsee.31.4.246-259.

10969845, 0, Downloaded from https://onlinelibrary.wiley.com/doi/10.1002/eqe.70154 by Tu Delft, Wiley Online Library on [17/03/2026]. See the Terms and Conditions (https://onlinelibrary.wiley.com/terms-and-conditions) on Wiley Online Library for rules of use; OA articles are governed by the applicable Creative Commons License

61. J. Liu, C. Zhai, P. Yu, C. Zhang, and H. Li, "Experimental and Numerical Analysis of Wheeled Medical Equipment With Adjacent Wall Subjected to Earthquakes," *Journal of Building Engineering* 72 (2023): 106635, https://doi.org/10.1016/j.jobe.2023.106635.

Supporting Information

Additional supporting information can be found online in the Supporting Information section.

Supporting File 1: eqe70154-sup-0001-SuppMat.pdf.

10969845, 0, Downloaded from https://onlinelibrary.wiley.com/doi/10.1002/eqe.70154 by Tu Delft, Wiley Online Library on [17/03/2026]. See the Terms and Conditions (https://onlinelibrary.wiley.com/terms-and-conditions) on Wiley Online Library for rules of use; OA articles are governed by the applicable Creative Commons License